Droplet Impact and Solidification in Plasma Spraying

69

Javad Mostaghimi and Sanjeev Chandra

Contents

Abstract

Plasma coatings are built up by agglomeration of splats formed by the impact, spread, and solidification of individual particles. Coating microstructure is determined by fluid flow and heat transfer during droplet impact. Coating properties such

J. Mostaghimi (✉)
Centre for Advanced Coating Technologies, Department of Mechanical and Industrial Engineering, Faculty of Applied Science + Engineering, University of Toronto, Toronto, ON, Canada
e-mail: mostag@mie.utoronto.ca

S. Chandra
Department of Mechanical and Industrial Engineering, University of Toronto, Toronto, ON, Canada
e-mail: chandra@mie.utoronto.ca

as porosity, adhesion strength, and surface roughness depend on the shape of splats and how they bond together and to the substrate. The splat shape is dependent on material properties of the powder, impact conditions (impact velocity and temperature), and substrate conditions (substrate roughness, material, temperature, and thermal contact resistance between the droplet and substrate). Coating adhesion strength increases by almost an order of magnitude as surface temperature is raised from room temperature to 650 °C. Increasing substrate temperature also changes the shape of splats formed by solidified droplets after impact on the surface. On a cold surface, there is splashing and droplet breakup, while splats on a hot surface are circular. Particle impact dynamics depends on the rate at which a droplet solidifies during impact, which is a function of substrate temperature, thermal contact resistance, and initial droplet temperature. Heating the surface affects droplet impact dynamics by changing thermal contact resistance, decreasing it by removing volatile compounds adsorbed on the surface. The trajectory of particles within the plasma and their residence time in the high-temperature zone determines their state at the point of impact: particles may be fully or partially melted with a few still completely solid.

1 Introduction

Plasma coatings are built up by agglomeration of splats formed by the impact, spread, and solidification of individual particles. Figure 1 shows a schematic diagram of a DC plasma spraying process. Inspection of a plasma coating cross section (Fig. 2) reveals that it is built up of thin lamellae formed by flattened droplets that land on each other and fuse together. These coatings are not fully dense since voids may be present at the interface between splats.

To ensure strong adhesion of a thermal spray coating, it is necessary to carefully prepare the substrate. Typically, the surface is roughened by grit blasting. Mechanical interlocking between solidified droplets and protrusions on the substrate produces strong bonding. Coating microstructure is highly dependent on fluid flow and heat transfer during droplet impact and is strongly affected by surface temperature.
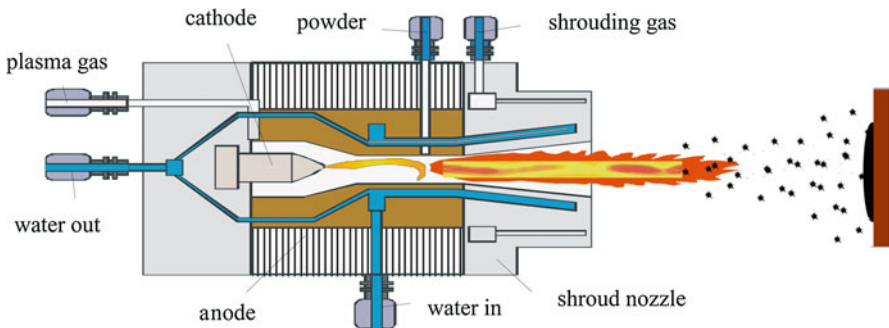

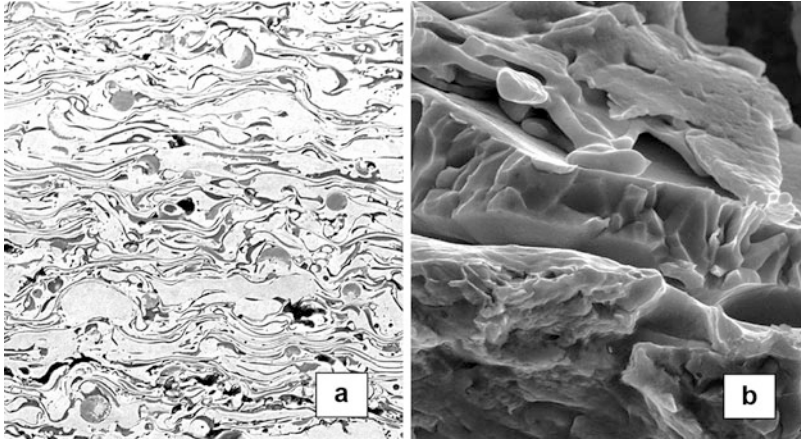**Fig. 1** Schematic of a DC plasma spray coating process

Fig. 2 A typical cross section of nickel-sprayed plasma coating (**a**), with higher magnification (**b**)

The effect of heat transfer and substrate condition on adhesion strength of plasma-sprayed coatings was demonstrated by Pershin et al. (2003). They sprayed nickel powder onto a stainless steel substrate and found that coating adhesion strength increased by almost an order of magnitude as surface temperature was raised from room temperature to 650 °C. Several explanations were offered: heating the surface removes volatile contaminants adsorbed on the surface, improving contact between impinging particles and the substrate, reducing the solidification rate of droplets allows them to flow into surface cavities before freezing, and enhancing mechanical bonding. The most visible effect of increasing substrate temperature, though, was to change the shape of splats formed by solidified droplets after impact on the surface. Figure 3 shows micrographs of splats produced by spraying nickel powder, sieved to give a size distribution of +63–75 µm, onto stainless steel surfaces maintained at either 290 °C (Fig. 3a) or 400 °C (Fig. 3b). Particle temperature in-flight was measured to be 1600 ± 220 °C and impact velocity 73 ± 9 m/s. On the colder surface, there was evidence of splashing and droplet breakup, while splats on the hotter surface were circular.

The effect of substrate temperature on splat shape has been well established in a number of studies, reviewed in detail by Fauchais and Fukumoto (2004). Fukumoto and Ohgitani (2004) performed a statistical analysis of splat shapes deposited on a surface and defined a "transition temperature" (T_t) as the substrate temperature where half of the splats on the surface were circular without splashing. Other researchers also observed this change of splat shape and showed that the transition temperature was a complex function of particle and substrate material properties (Zhang and Wang 2001), surface contamination (Li et al. 1998), and surface oxidation (Pech and Hannoyer 2000). Jiang and Wan (2001) plasma sprayed molybdenum onto polished stainless steel coupons and found that increasing impact velocity enhanced splashing; removing adsorbed volatile compounds on the surface reduced splashing. Fukomoto and Huang (1999) suggested that freezing along the bottom of an impinging droplet causes splashing: liquid flowing on top of the solid layer jets off and splashes.
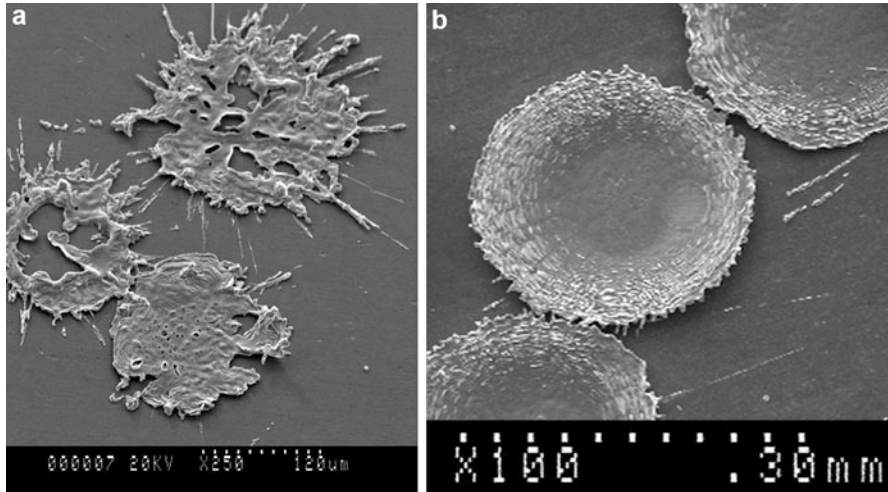
Fig. 3 Splats formed by spraying molten nickel particles on a stainless steel surface initially at (**a**) 290 °C and (**b**) 400 °C. The particle size distribution was $-53 + 63$ μm, particle temperature before impact 1600 ± 220 °C, velocity 73 ± 9 m/s

Particle impact dynamics depends on the rate at which a droplet solidifies during impact, which is a function of the heat flux from the molten droplet to the substrate. When molten metal comes suddenly in contact with a rough, solid surface, air may be trapped in crevices at the liquid-solid interface, creating a temperature difference between the molten metal and the substrate, whose value depends on surface finish, contact pressure, and material properties. To quantify the magnitude of this effect, the thermal contact resistance (R_c) is defined as the temperature difference between the droplet (T_d) and substrate (T_s) divided by the heat flux (q'') between the two:

$$R_c = \frac{T_d - T_s}{q''} \tag{1}$$

Droplet solidification rate is therefore a function not just of substrate temperature but also of contact resistance and initial droplet temperature. Heating the surface indirectly affects droplet impact dynamics by changing thermal contact resistance, either decreasing it by removing volatile compounds adsorbed on the surface or possibly increasing it in the case of metallic substrates heated in air, due to the formation of an oxide layer. If nickel particles are plasma sprayed onto a steel surface that is at room temperature, they will splash, but not on a surface that is maintained at 400 °C; however, splashing is also suppressed on a surface that is heated to 400 °C in air, oxidized, and then cooled (Pershin et al. 2003).

Computer simulations of impacting molten metal droplets, Mehdizadeh and Raessi (2004) provide insight into a mechanism for solidification-induced splashing. A spreading drop begins to freeze along its edges, where it first contacts the colder substrate. The solid rim formed obstructs further flow, forcing liquid to jet off the

surface so that it becomes unstable and breaks up into satellite droplets. Reducing heat transfer from the droplet slows solidification and allows the droplet to spread into a disk before freezing. It was found in simulations that the rate of solidification was much more sensitive to values of thermal contact resistance than substrate temperature. Simulations of impact of nickel particles, Mostaghimi et al. ([2002](#)) showed that raising substrate temperature from 290 °C to 400 °C had little effect on impact dynamics, but increasing thermal contact resistance from 10^{-7} to 10^{-6} m²K/W diminished heat transfer sufficiently to prevent splashing. An oxide layer or adsorbed contaminants on the surface may, in practice, alter thermal contact resistance.

The state of particles at the point of impact is important in the type of microstructure the coating will have, and it is dependent on the trajectory of particles and their residence time within the plasma. Thus, the particles may be fully or partially melted with a few still completely solid. Coating properties such as porosity, adhesion strength, and surface roughness depend on the shape of these splats and how they bond together and to the substrate. The splat shape is dependent on material properties of the powder, impact conditions (e.g., impact velocity and temperature), and substrate conditions, e.g., substrate roughness, material, temperature, and contact resistance.

The next few sections will review the dynamics of impact and solidification in thermal spray processes and the effect of impact parameters on the final shape of splats.

2 Droplet Impact, Spread, and Solidification

Individual splats are the building blocks of thermal spray coatings. The shapes of these splats are a function of particle impact conditions, physical properties of the powder and substrate, and substrate temperature, roughness, and chemistry. To better understand coating formation, we need to investigate the following topics:

1. Relationship between the final splat shape and impact parameters, thermophysical properties of the powder, substrate thermal properties, and substrate roughness
2. Splashing and breakup of impacting fully or partially molten droplets
3. Interaction of splats on the substrate

Prediction of splat shapes involves numerical simulation of fluid flow and heat transfer of an impacting droplet. In general, this is a three-dimensional, time-dependent problem. One challenge is the prediction of rapid and large deformations of impacting droplets and their simultaneous solidification on the substrate.

2.1 Axisymmetric Impact

Consider the isothermal normal impact of a spherical droplet on a smooth, flat surface, as shown in Fig. [4](#). Furthermore, assume the gas phase is passive and does not influence the impact. The parameters that affect the impact are initial

Fig. 4 Schematic of droplet impact
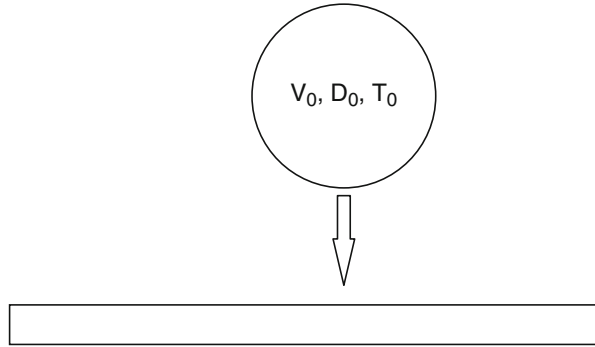
droplet diameter D_0, impact velocity V_0, droplet density ρ, liquid viscosity μ, liquid-gas surface tension σ, and liquid-solid contact angle θ. Combining these into nondimensional groups reduces the number of variables to three: contact angle and the Reynolds and the Weber numbers,

$$\mathrm{Re} = \frac{\rho V_o D_0}{\mu} \quad , \quad We = \frac{\rho V_0^2 D_0}{\sigma} \tag{2}$$

There have been many successful attempts to derive analytical expressions for the extent of maximum spread, $\xi_{\max} = D_{\max}/D_0$, as a function of process variables (Madejski 1976; Pasandideh-Fard et al. 1996). In the absence of solidification, and with the condition of $We \gg \sqrt{\mathrm{Re}}$ and $We \gg 12$, which is normally the case in spray coating process, a simple formulation for the degree of maximum spread is obtained,

$$\xi_{\max} = a\, Re^b \tag{3}$$

where a = 1.293, b = 1/5 (Madejski 1976), or a = 0.5, b = 1/4 (Pasandideh-Fard et al. 1996).

Pasandideh-Fard et al. (1998) developed a simple model to predict the maximum spread diameter of an impacting droplet. In this model, they equated the energy before and after impact, accounting for the energy dissipation during impact. The initial kinetic energy (KE_1) and surface energy (SE_1) of a liquid droplet before impact are,

$$KE_1 = \left(\frac{1}{2}\rho V_o^2\right)\left(\frac{\pi}{6}D_o^3\right) \tag{4}$$

$$SE_1 = \pi D_o^2 \sigma \tag{5}$$

After impact, when the droplet is at its maximum extension, the kinetic energy is zero, and the surface energy (SE_2) is approximately,

$$SE_2 = \frac{\pi}{4} D_{max}^2 \sigma (1 - \cos \theta_a) \tag{6}$$

where θ_a is the advancing liquid-solid contact angle. The work done in deforming the droplet against viscosity (W) is approximately,

$$W = \frac{\pi}{3} \rho V_o^2 D_o D_{max}^2 \frac{1}{\sqrt{Re}} \tag{7}$$

The effect of solidification in restricting droplet spread is modeled by assuming that all the kinetic energy stored in the solidified layer is lost. If the solid layer has average thickness s and diameter d_s when the splat is at its maximum extension, then the loss of kinetic energy (ΔKE) is approximated by,

$$\Delta KE = \left(\frac{\pi}{4} d_s^2 s \right) \left(\frac{1}{2} \rho V_o^2 \right) \tag{8}$$

d_s varies from 0 to D_{max} during droplet spread: a reasonable estimate of its mean value is $d_s \sim D_{max}/2$. Substituting Eqs. 4–8 into the energy balance, $KE_1 + SE_1 = SE_2 + W + \Delta KE$ yields an expression for the maximum spread factor,

$$\xi_{max} = \frac{D_{max}}{D_o} = \sqrt{\frac{We + 12}{\frac{3}{8} We s^* + 3(1 - \cos \theta_a) + 4 \frac{We}{\sqrt{Re}}}} \tag{9}$$

where s^* is the dimensionless solid layer thickness ($s^* = s/D_o$).

There are two unknowns in Eq. 9: advancing contact angle (θ_a) and solidified layer thickness (s^*). Liquid-solid contact angles during spreading and recoil of tin droplets on a stainless steel were measured from enlarged photographs by Aziz and Chandra (2000), and the advancing contact angle was found to be almost constant at $\theta_a = 140°$.

The growth in thickness of the solidified layer can be calculated using an approximate analytical solution developed by Poirier and Poirier (1994). The model assumes that heat transfer is by one-dimensional conduction; there is no thermal contact resistance at the droplet-substrate interface; the temperature drop across the solid layer is negligible; the substrate is semi-infinite in extent and has constant thermal properties. The dimensionless solidification thickness was expressed as a function of the Stefan number ($Ste = C(T_m - T_{w,i})/H_f$, where T_m is the melting temperature of the droplet, $T_{w,I}$ the initial substrate temperature, and H_f the latent heat of fusion), Peclet number ($Pe = V_o D_o/a$), and $\gamma = k\rho C$,

$$s^* = \frac{2}{\sqrt{\pi}} Ste \sqrt{\frac{t^* \gamma_w}{Pe \gamma_d}} \tag{10}$$

Fig. 5 Calculated (*lines*) and measured (*symbols*) variation of maximum spread factor with impact velocity for 2.0-mm-diameter tin droplets landing on a stainless steel surface with initial temperature $T_{w,i}$
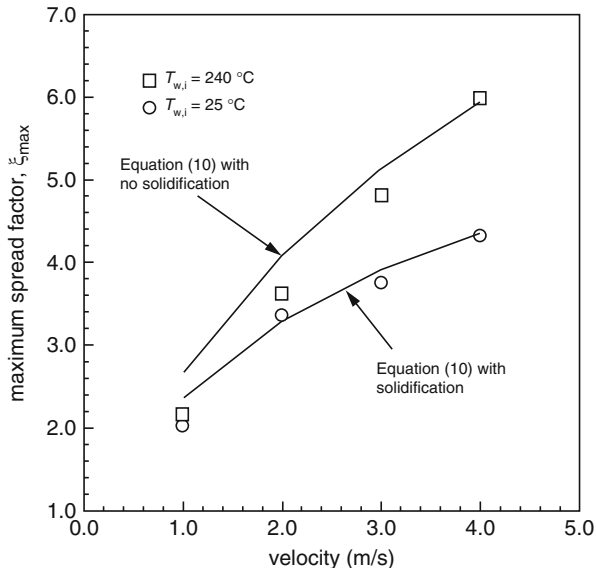
The nondimensional time to arrive at the maximum spread is shown by Pasandideh-Fard et al. (1998) to be approximately $t^* = 8/3$. Substituting Eq. 10 into Eq. 9 gives the maximum spread of a droplet that is solidifying during impact,

$$\xi_{max} = \sqrt{\frac{We + 12}{We\,Ste\sqrt{\frac{3\gamma_w}{2\pi Pe\gamma_d}} + 3(1 - \cos\theta_a) + 4\left(\frac{We}{\sqrt{Re}}\right)}} \qquad (11)$$

The variation of ξ_{max} with impact velocity predicted by Eq. 11 for droplets falling on a substrate at 25 °C is shown in Fig. 5, along with measured values. Predictions of ξ_{max} from Eq. 11, for a droplet spreading without solidifying, are also compared with measurements for droplets impacting a surface at 240 °C. Agreement between measured and calculated values is good in both instances. At low impact velocity, Eq. 11 predicts somewhat larger values of ξ_{max} than were measured. To estimate viscous dissipation, the model assumes that there exists a thin boundary layer in the drop which is not true when the droplet is deposited very gently. The effect of solidification on droplet spreading can be estimated from Eq. 11. In thermal spraying, the second term in the denominator of Eq. 11 is negligible. The ratio of the first to last term in the denominator will provide a measure of the importance of solidification on the dynamics of droplet impact. Aziz and Chandra (2000) proposed that if the following nondimensional parameter is much less than unity, solidification effect on the extent of droplet spread is negligible,

$$\Phi = \frac{Ste}{\sqrt{Pr}} \sqrt{\frac{\gamma_w}{\gamma_d}} \ll 1 \tag{12}$$

The above analytical relations are quite useful in approximately describing the relation between maximum spread and impact variables, and they provide some information about potential breakup upon impact. Modeling breakup and splashing and interaction of splats on the substrate require more detailed numerical models.

To better understand the dynamics of impact, spread, and solidification, a number of two-dimensional, axisymmetric models were initially developed. Zhao et al. (1996a, b) studied, both experimentally and numerically, heat transfer and fluid flow of an impacting droplet. Solidification was not considered in this work. Bennet and Poulikakos (1994) and Kang et al. (1994) studied droplet deposition assuming solidification to start after spreading is completed. As discussed above, the validity of this assumption depends on both Prandtl and Stefan numbers. Liu et al. (1993), Bertagnolli et al. (1995), and Trapaga et al. (1992) numerically studied solidification and spreading of the impacting drops. The substrate was assumed to be isothermal. Additionally, the important effect of thermal contact resistance between the drop and the substrate was ignored. The liquid-solid contact angle was also considered to be constant, with an arbitrarily assigned value. Pasandideh-Fard et al. (1996), however, showed that the value of contact angle can have a significant effect on the results.

Pasandideh-Fard and Mostaghimi (1996) studied the effect of thermal contact resistance between the droplet and the substrate. They showed that its magnitude could have a dramatic effect on droplet spreading and solidification. Solidification and heat transfer within the substrate were modeled assuming one-dimensional heat conduction. The model was later completed, and a fully two-dimensional axisymmetric model of droplet impact was developed, and impact and solidification of relatively large tin droplets (~2 mm diameter) on stainless steel substrates were studied both numerically and experimentally (Pasandideh-Fard et al. 1998). The model correctly predicted the shape of the deforming droplet. The values of thermal contact resistance were estimated by matching the numerical predictions of substrate temperature with those measured experimentally. While thermal contact resistance should, in principle, vary at different contact points, it was shown that accurate simulations of the impact could be done using a constant value. The results also showed the sensitivity of the predicted maximum spread to the value of thermal contact resistance.

A few experimental studies have investigated the impact of molten droplets. Inada and Yang (1994) measured the temperature variation of a plate on which a molten lead droplet was dropped and concluded that the droplet cooling rate was a function of impact velocity. Watanabe et al. (1992) photographed impact of n-cetane and n-eicosane droplets on a cold surface and concluded that in their tests, droplets spread completely before solidifying. Fukanuma and Ohmori (1994) photographed the impact of tin and zinc droplets and also found that freezing had no influence on droplet spread. Inada and Yang (1994) used holographic interferometry to observe droplet-substrate contact during impact of lead droplets on a quartz plate.

Liu et al. (1995) measured the temperature variation on the upper surface of an impacting metal droplet by a pyrometer and used these results to estimate the thermal resistance under the drop. However, the response time of the pyrometer (25 ms) was longer than the time taken by the droplet to spread, so that their results are applicable to the period after the droplet had come to rest rather than the duration of the impact itself. Pasandideh-Fard et al. (1998) photographed the impact of tin droplets on a stainless steel substrate and measured the changes in substrate temperature during the impact. They showed that the value of the maximum spread is sensitive to the magnitude of thermal contact resistance, which in their case was estimated from the measurements.

2.2   Droplet Splashing

When a droplet impacts a solid surface, it spreads into a thin circular sheet. If the impact velocity is sufficiently large, fluid instabilities create undulations around the edge of the spreading sheet that grow larger and form fingers. The fingers detach and form satellite droplets, a process that is commonly known as "splashing."

The first experimental study of droplet fingering and splashing – in the absence of solidification – was that of Worthington (1876, 1907) which was published over a century ago. He observed that the number of fingers increased with droplet size and impact speed, observed merging of the fingers at or soon after the maximum spread, and found fingering to be more pronounced for fluids that did not wet the substrate. Many researchers have since contributed to the understanding of the fingering and splashing in the absence of solidification. A review of their findings may be found in the works of Bussmann et al. (1999, 2000) and Bussmann (1999).

Aziz and Chandra (2000) proposed a simple model based on the Rayleigh-Taylor instability and showed that in the absence of solidification, the number of fingers around the impacting droplet is,

$$N = \frac{K}{4\sqrt{3}} \tag{13}$$

where $K = \sqrt{We\sqrt{Re}}$ is the so-called splash parameter. The above derivation assumes that $We \gg 12$ and $\frac{We}{\sqrt{Re}} \gg 1$. These two conditions are satisfied in the thermal spray coating process. When solidification is included in the analysis, the number of fingers at the maximum spread is,

$$N = \sqrt{\frac{We}{12}\left(\frac{We + 12}{We\ Ste\sqrt{\frac{3\gamma_w}{2\pi Pe\gamma_d}} + 3(1 - \cos\theta_a) + 4\left(\frac{We}{\sqrt{Re}}\right)}\right)} \tag{14}$$

Fig. 6 Calculated (*lines*) and measured (*symbols*) variation of maximum spread factor with impact velocity for 2.0-mm-diameter tin droplets landing on a stainless steel surface with initial temperature $T_{w,i}$ (Aziz and Chandra)
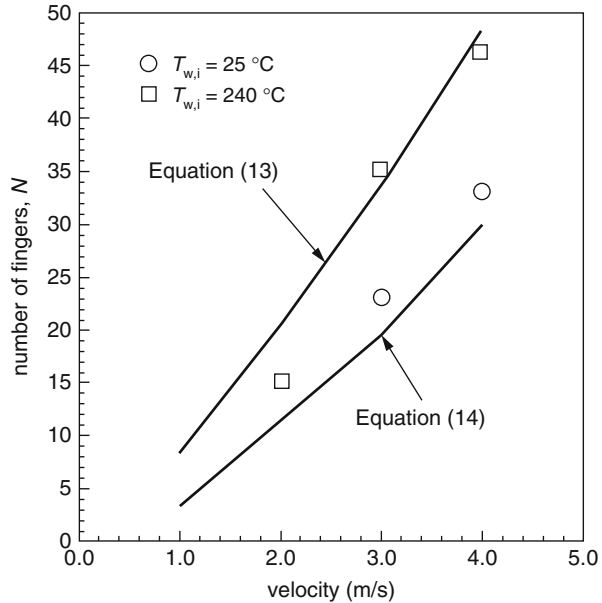

Figure 6 shows a comparison of the predicted number of fingers by Eqs. 13 and 14 and experiments for two substrate temperatures.

Bussmann et al. (2000) developed a three-dimensional model for the isothermal impact of a droplet on a solid surface. The model employs a fixed-grid Eulerian approach along with a volume tracking algorithm to track fluid deformation and droplet-free surface. Pasandideh-Fard et al. (2002a) extended this model to include heat transfer and solidification. This model is described in the next section.

Some of the difficulty in predicting when splashing will occur can be attributed to uncertainties about surface wettability and the effect of the surrounding atmosphere. However, the term "splashing" has been used to refer to several different mechanisms that lead to breakup of droplets after impact. Rioboo et al. (2001) identified three different types of splashing. Immediately after impact, as the liquid sheet under the droplet spreads out, its edge becomes unstable and fingers around the edge begin to break off and form small droplets. This has been termed "prompt splash" and occurs when the edge of the lamella is still in contact with the surface.

The second type of splashing has been termed "corona" splashing: the liquid lamella lifts off the surface; the edge becomes unstable so that fingers grow at regular spaced intervals and their tips break off in the crown-like shape characteristic of splashing drops. Many studies have been devoted to predicting when corona splashes will occur. Mundo et al. (1995) found that droplets splashed only if the so-called splash parameter $K = We^{1/2}Re^{1/4}$ exceeds a critical value $K = 57.7$. Cossali et al. (1997) developed an empirical correlation between K, surface roughness R_a, and the liquid lamella thickness h.

The air film trapped under the impacting droplet plays an important role in creating instabilities. Xu et al. (2005) demonstrated that if the pressure in the atmosphere surrounding an impacting drop is reduced, corona splashes are suppressed. Prompt splashing, however, persists even in the absence of surrounding gas (Xu et al. 2007).

The third type of splashing is known as "receding breakup," in which the droplet remains intact until it has spread to its maximum extent, and then, as surface tension forces pull it back, the fingers formed due to instabilities around its periphery grow longer and begin to break up into smaller droplets. If the liquid-solid contact angle is small, less than 90°, neighboring fingers along the edges of the spreading liquid sheet tend to merge with each other and disappear. However, if the contact angle is large, as is the case with droplets of molten metal, the cylindrical fingers become unstable and disintegrate.

Apart from these three mechanisms, there are two others that can cause breakup of impacting droplets. If a droplet impacts on a substrate that is cold enough to cause freezing, the solid layer formed at the liquid-substrate interface acts as a barrier. The spreading liquid hits the solid mass obstructing its path, jets upward, and disintegrates. This is known as freezing-induced splashing (Dhiman and Chandra 2005) and whether it occurs depends on the rate of heat transfer between the droplet and substrate, which is controlled by the substrate temperature, substrate thermal properties, and the thermal contact resistance at the liquid-solid interface.

Finally, if impact velocities are very high, the liquid film may become very thin so that air trapped under it breaks through. These holes in the liquid grow larger and can eventually lead to complete disintegration of the droplet (Mehdizadeh et al. 2005).

2.3   Photographing Plasma Particle Impact

McDonald et al. (2006) photographed the impact of plasma-sprayed molybdenum and amorphous steel particles (38–55 μm diameter) during impact (velocity 120–200 m/s) and spreading on a smooth glass surface that was maintained at either room temperature or 400 °C. Figure 7 shows a schematic diagram of the experimental apparatus used. A plasma torch was passed rapidly across the glass substrate that was protected from heat by a series of barriers with holes in them through which a few particles could pass. After exiting the third barrier and just before impacting the substrate, the thermal radiation of the particle was measured with a rapid two-color pyrometric system consisting of an optical sensor head which focused the collected radiation on an optical fiber covered with a mask that was opaque except for three slits (see Fig. 8). The two smaller slits (slits b and c in Fig. 8a) were used to detect thermal radiation emitted by particles while they were still in flight, from which their temperature, velocity, and diameter could be calculated. The largest slit (slit e in Fig. 8a) was used to collect thermal radiation of the particle as it impacted and spread on the substrate. With the thermal radiation from this slit, the splat temperature, diameter, and cooling rate were calculated at 100 ns intervals after impact.

Figure 8b shows a typical signal captured by a photodetector. The labels, *a–f*, correspond to the position of a particle (shown in Fig. 8c) as it passes through the fields of view of each of the optical slits. At points *a* and *d*, the particle was not in the
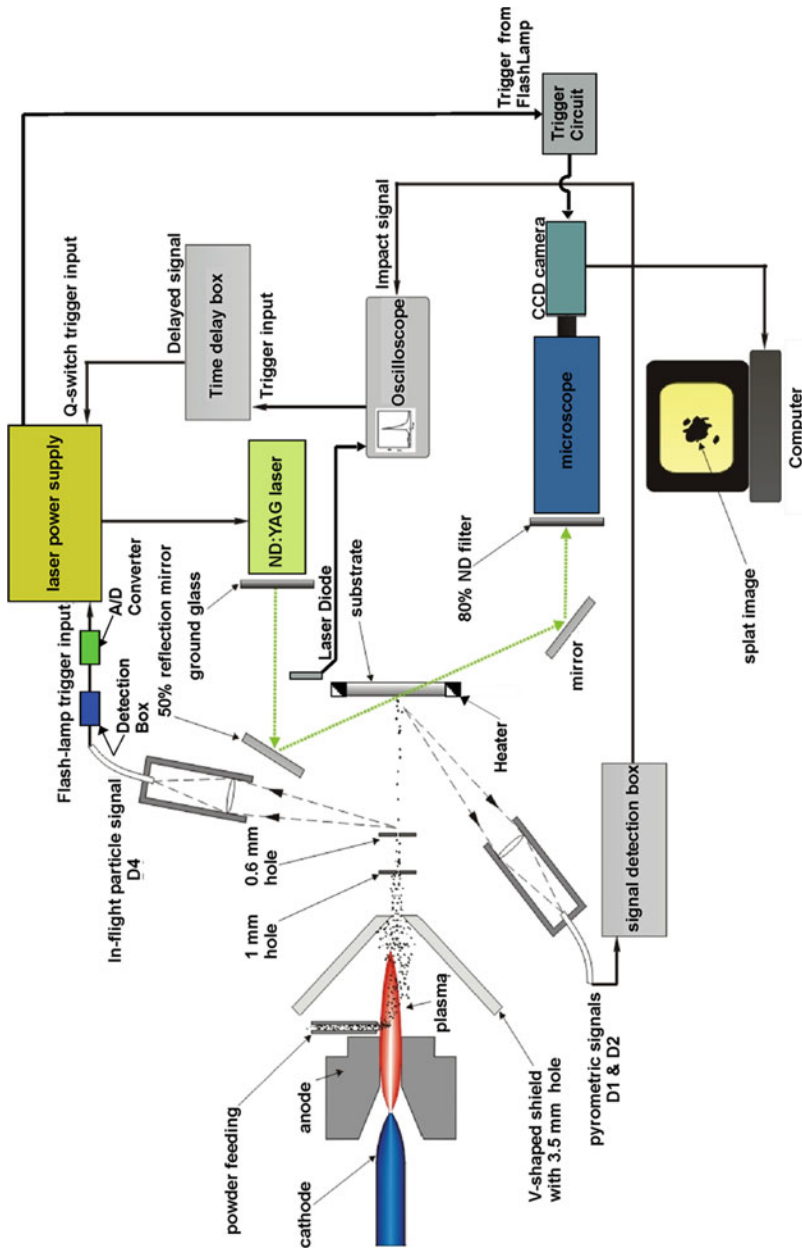
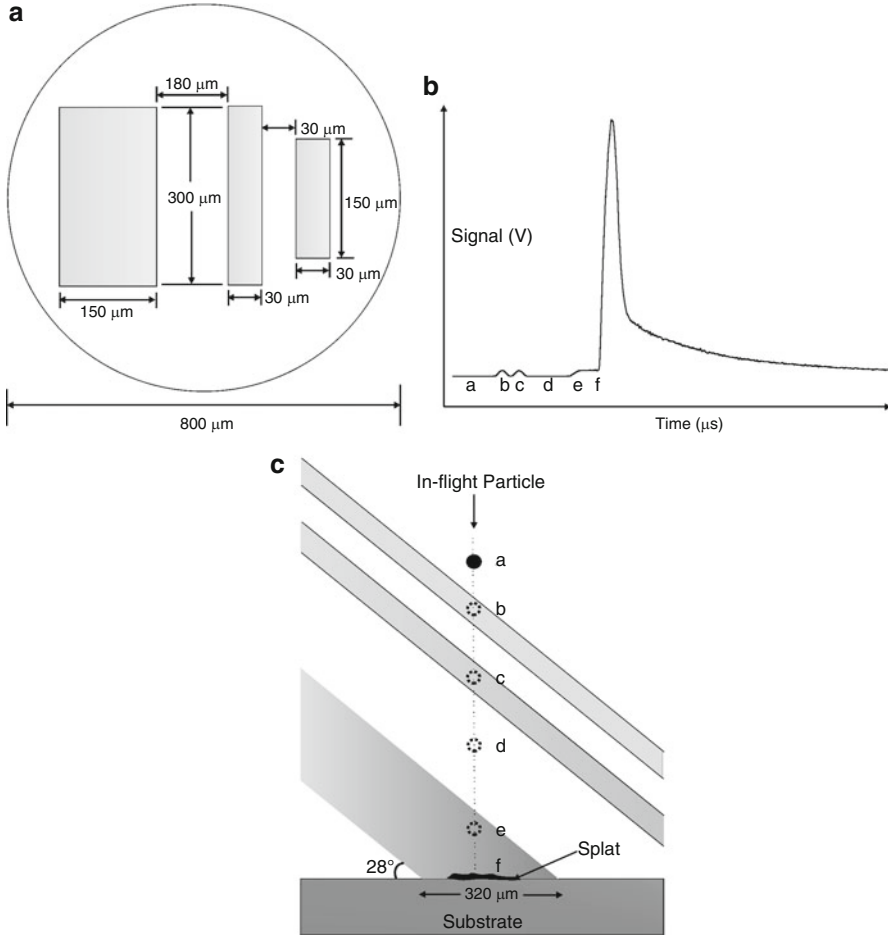**Fig. 7** Schematic of the experimental assembly [G]

a

b

c

Fig. 8 (**a**) Details of the three-slit mask, (**b**) a typical signal collected by the three-slit mask, (**c**) schematic of the optical detector fields of view [G]

optical field of view of any of the slits, so the signal voltage was zero. The two peaks at points b and c were produced by thermal emissions from the particle as it passed through the first two small slits. The droplet average in-flight velocity was calculated by dividing the known distance between the centers of the two slits by the measured time of flight. At point e, the droplet entered the field of view of the third and largest optical slit. This is shown on the thermal signal by a plateau in the profile. Upon impact at f, the signal increased as the particle spread and eventually decreased as the particle cooled down and/or splashed out of the field of view. A CCD camera was used to capture images of the spreading particles from the back of the glass substrate. The electronic shutter of the camera was triggered to open by a signal from the flashlamp of the laser.

Figure 9a shows images of molybdenum splats at different times after impact on glass held at room temperature or at 400 °C. The figure also shows the corresponding thermal emission signals. For molybdenum, the average droplet diameter was 40 μm, the average impact velocity was 135 m/s, and the average temperature of the particles in flight was 2980 °C, well above the melting point (2617 °C). The photodetector signal of impact and spread on the glass held at room temperature was subdivided into four intervals (indicated by labels *a–e* in Fig. 9a), and photographs taken in each of these time periods are grouped together in Fig. 9. The approximate time after impact that corresponds to each interval is shown in the figure. To demonstrate the repeatability of the process, two splat images are shown during each time interval. The *a* to *b* range represents splats immediately before or upon achieving the maximum spread diameter of 400 μm. Beyond point *b*, the liquid portion of the splats begins to disintegrate, initially from the solidified central core, and later, from sites within the liquid film. After point *d*, the splat is almost totally disintegrated and only a central solidified core remains on the glass. Figure 9b shows the results after impact on a glass substrate at 400 °C. There was almost no splat breakup or splashing, unlike that seen in Fig. 9a.

The time required for the splat to spread to its maximum diameter after impact was measured starting at the instant the pyrometric thermal emission signals began to increase after the plateau (point *f* of Fig. 9b) to the maximum voltage on the thermal emission signal profile. For molybdenum on glass held at room temperature, the maximum spread time was 2 μs and on glass held at 400 °C, it was 1 μs.

The evolution of the liquid temperature during the spreading of molybdenum splats on cold and hot glass is illustrated in Fig. 10. The average slope of the curves (dT/dt) represents the splat cooling rate. The liquid cooling rate on a glass surface held at 400 °C is approximately an order of magnitude larger ($\sim 10^8$ K/s) than on a surface held at room temperature ($\sim 10^7$ K/s) demonstrating that thermal contact resistance between the splat and the cold glass is greater than that between it and the hot glass. The cause of the increased thermal contact resistance on the cold surface is probably a gas barrier, formed after evaporation of adsorbed substances on the substrate beneath the splat. Heating the surface removes the adsorbed substances, producing better contact. McDonald et al. (2007) developed a one-dimensional heat conduction model to estimate the magnitude of thermal contact resistance and estimated it to be 4.9×10^{-5} m^{2}K/W for molybdenum splats impacting a glass surface at room temperature, while it was 6.5×10^{-7} m^{2}K/W for a glass surface at 400 °C. Table 1 summarizes the results of these experiments.

2.4   Splat Shapes

Impacting plasma spray particles may fragment due to two different mechanisms. If the thermal contact resistance under the splat is very low, and cooling is very rapid, it begins to solidify as it spreads. The solid layer obstructs and destabilizes the flow of liquid, leading to fingers being formed around its edges. At the other extreme, if contact resistance is very high, the particle remains liquid and spreads into a very
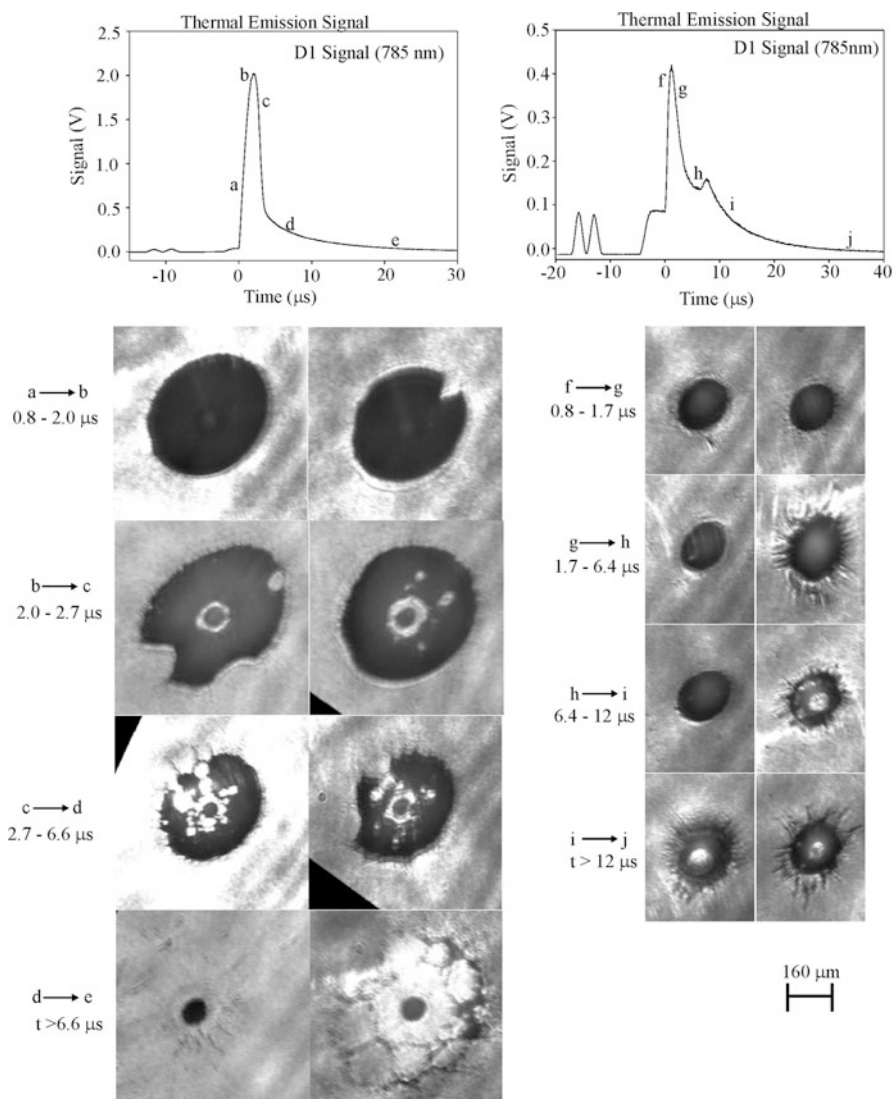
Fig. 9 Typical thermal emission signals and images of molybdenum splats at different times after impact on glass held at (**a**) room temperature and (**b**) 400 °C [G]

thin film that ruptures internally. In this case, the splat is also fragmented, but its shape is different, appearing as a small central core surrounded by a ring. Disk-shaped splats are formed if the value of thermal contact resistance lies between these two extremes, so solidification starts after the particle has already flattened out and does not obstruct the liquid flowing outward, but is still sufficiently rapid to prevent the splat from spreading so thin that it ruptures internally.

Fig. 10 Typical cooling curves of molybdenum splats on glass held at (**a**) room temperature and (**b**) 400 °C [G]
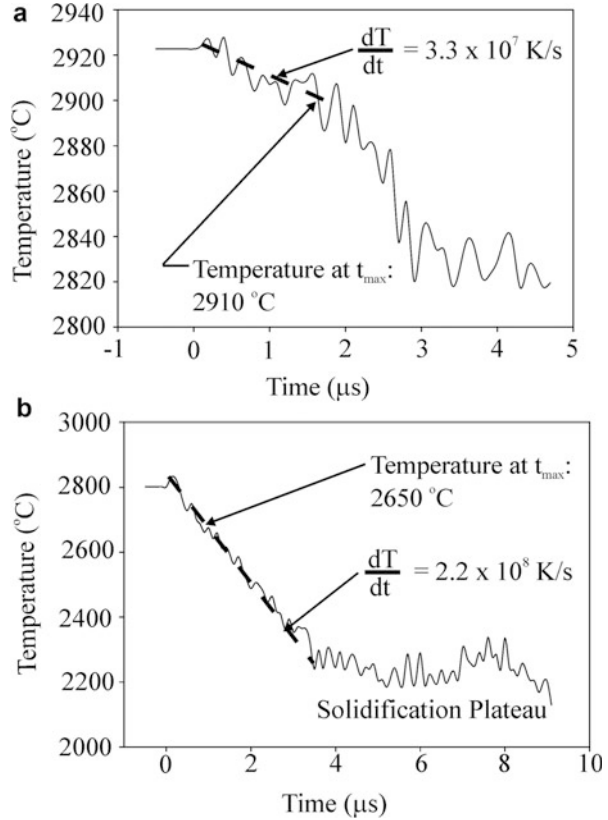

Table 1 Average cooling rates of molybdenum and amorphous steel splats

Material	Glass temperature(°C)	No. of samples	$\frac{dT}{dt} \times 10^7 (\mathrm{K/s})$
Molybdenum	27	17	3.3 ± 0.2
	400	21	22 ± 1.2
Amorphous steel	27	12	5.8 ± 0.8
	400	6	32 ± 1.7

Dhiman et al. (2007) proposed a single parameter to estimate the importance of freezing during solidification and predict the likelihood of splat breakup. When a molten droplet lands on a solid surface, it spreads into a thin splat of uniform thickness h. If the substrate is at a temperature lower than the melting point of the droplet, a solid layer of thickness s grows in it during the time it takes to reach its maximum spread. The solidification parameter is defined as the ratio of the solid layer thickness to splat thickness ($\Theta = s/h$). Dhiman et al. (2007) developed an analytical expression to calculate the value of Θ as a function of the droplet impact parameters. The magnitude of Θ can be used to predict what the final shape of the splat will be and what the mechanism of break up, if it occurs, is. Three outcomes are possible during spreading:

1. A very thin solid layer ($\Theta \ll 1$) has no effect on spreading. The splat spreads into a thin sheet of liquid, ruptures internally, and fragments, producing a small central splat surrounded by a ring of debris.
2. If solid layer growth is significant ($\Theta \sim 0.1\text{–}0.3$), it will restrain the splat from spreading too far and becoming thin enough to rupture, producing a disk-type shape.
3. If solidification is very rapid ($\Theta \sim 1$), the solid layer obstructs the outward spreading liquid and produces a splat with fingers radiating out from its periphery.

Comparison with experimental photographs, Dhiman et al. (2007) showed the value of the solidification parameter gave a reasonably accurate method of predicting the shape of the final splat. Figure 11 shows photographs of splats taken both during and after impact, illustrating the three different modes of droplet impact. In Fig. 11a, for molybdenum and nickel particles landing on substrates at room temperature, thermal contact resistance was high ($\sim 10^{-5}$ m^{2}K/W) and $\Theta \sim 0.01$. The splats spread into a thin film that ruptured internally and fragmented. The final splats all showed a central portion at the point of impact that adhered strongly to the substrate, surrounded by a ring.

Raising the substrate temperature reduced the thermal contact resistance by an order of magnitude, since it evaporated adsorbed contaminants on the surface. Figure 11b shows impact of zirconia and nickel particles on surfaces heated to 400 °C which had $R_c \sim 10^{-6}$ m^2 K/W and correspondingly $\Theta \sim 0.1$. Solidification occurred near the end of droplet flattening, when the spreading liquid did not have enough momentum to jet over the solid rim and instead came to rest forming a circular splat with smooth edges.

If Θ was increased further ($\Theta \sim 0.4$, see Fig. 11c), solid layer growth was sufficiently rapid to obstruct flow of liquid early during spreading. The liquid had enough momentum that it jetted outward, producing fingers radiating out from the central splat. For nickel particles spreading on a steel substrate oxidized by heating to 640 °C (Fig. 11c), the splat was intact, and smooth at the center, where solidification was slow. The edges, which solidified very rapidly, have a rough surface since surface tension did not have time to level irregularities before solidification occurred. Molybdenum splats on a glass surface heated to 400 °C also have fingers radiating out.

3   Mathematical Model of Impact

3.1   Fluid Flow

Assume that the droplet is spherical at impact, the liquid is incompressible, and flow is Newtonian and laminar, shear at the free surface is negligible. Finally, droplet properties are assumed to be constant.

3.1.1   Governing Equations

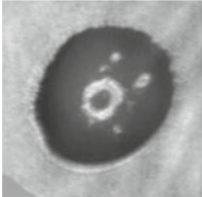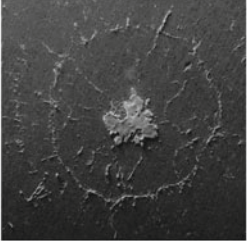The equations governing the conservation of mass and momentum in an Eulerian frame of reference are,
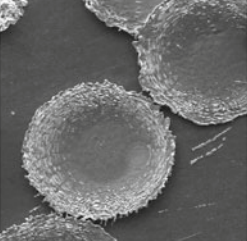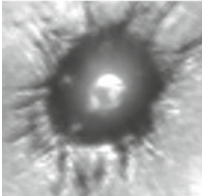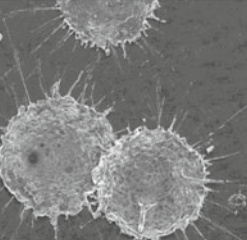
	Splat Impact Mode	Pictures during impact	Splat images
(a)	**Fragmentation** (Slow solidification) $\Theta \sim 0.01$	Mo on glass, room temp	Ni on steel, room temp
(b)	**Disk Splats** (Intermediate rate of solidification) $\Theta \sim 0.1$	ZrO$_2$ on glass, 400°C	Ni on steel 400°C
(c)	**Freezing induced break-up** (Rapid solidification) $\Theta \sim 0.4$	Mo on glass, 400°C	Ni on steel 640°C

Fig. 11 Photographs during and after impact for splats (**a**) fragmenting during impact, (**b**) forming disk splats, and (**c**) undergoing freezing-induced breakup [J]

$$\frac{\partial \rho}{\partial t} + \nabla \cdot (\rho \mathbf{V}) = 0 \tag{15}$$

$$\frac{\partial (\rho \mathbf{V})}{\partial t} + \nabla \cdot (\rho \mathbf{V V}) = -\nabla \mathrm{p} + \nabla \cdot \overline{\overline{\tau}} + F_b + F_{ST} \tag{16}$$

where V is the velocity vector, ρ is the fluid density, p is the pressure, $\overline{\overline{\tau}}$ is the shear stress tensor, F_b represents body forces such as gravity acting on the fluid elements, and F_{ST} is the surface tension force which acts only near the fluids interface (Brackbill et al. 1992). Assuming the fluids are Newtonian, the shear stress tensor is expressed,

$$\overline{\overline{\tau}} = \mu \left(\nabla \mathbf{V} + \nabla \mathbf{V^T} \right) \tag{17}$$

where μ is the dynamic viscosity. Using the one-field approach and having several fluids in the domain, each with velocity field V_k, we may assume that all fluids move with the local center of mass velocity V, Kothe (1998),

$$V_k = V \tag{18}$$

3.2 Interface Tracking

There are a number of methods described in the literature to resolve the interface between two immiscible and incompressible fluids. These include the volume of fluid (VOF) method (Hirt and Nichols 1981), level set (LS) method (Osher and Fedkiw 2001), coupled level set volume of fluid (CLSVOF) method, height function (HF) method (Afkhami and Bussmann 2008), and volume of fluid with advecting normal (VOF-AN) method (Raessi et al. 2007).

One of the most common and robust approaches for tracking interfaces is the volume of fluid (VOF) approach. In this method, a scalar function f is defined to mark the space where each fluid resides. In the case of two immiscible fluids, the values are assigned zero in one fluid and unity in the second one. Since all fluids are assumed to be incompressible, f is passively advected with the flow and, thus, it satisfies the advection equation,

$$\frac{\partial f}{\partial t} + V \cdot \nabla f = 0 \tag{19}$$

where

$$f\left(\vec{r}\right) = \begin{cases} 1, & \vec{r} \in \text{fluid 1} \\ 0, & \vec{r} \in \text{fluid 2}. \end{cases} \tag{20}$$

$\vec{r}$ is the position vector. The interface normal and curvature can be calculated from the VOF data by,

$$\hat{n} = \frac{\nabla f}{|\nabla f|} \tag{21}$$

$$\kappa = -\nabla \cdot \hat{n} \tag{22}$$

The numerically discretized form of f is the fraction of a numerical control volume occupied by fluid 1, i.e.,

$$F = \frac{1}{V} \int_V f \, dv \tag{23}$$

Thus $f = 1$ in cells that are fully occupied by fluid 1 and $f = 0$ for cells that are filled with fluid 2. Thus $0 < F < 1$ for those cells that contain both fluids. Eq. (19) is numerically solved using the Youngs algorithm (Bussmann et al. 1999).

Based on the volume fraction of each phase, mixture properties in the interface cells are defined,

$$
\begin{aligned}
\rho &= f\rho_d + (1-f)\rho_b \\
\mu &= f\mu_d + (1-f)\mu_b \\
\kappa^{-1} &= f/\kappa_d + (1-f)/\kappa_b
\end{aligned}
\tag{24}
$$

where d and b refer to dispersed and bulk phases, respectively. The surface tension force, F_{ST}, which is nonzero only at the interface, can be expressed,

$$
F_{ST} = \sigma(T)\kappa\nabla f + \nabla_\parallel \sigma(T)\,|\nabla f| \cong \sigma(T)\kappa\nabla f
\tag{25}
$$

where κ is the local interface curvature, T is the interface temperature, and $\nabla_\parallel$ is the tangential surface derivative. The first term on the right-hand side corresponds to the temperature-dependent normal surface tension component, while the second term corresponds to the Marangoni force. The Marangoni convection force is negligible during droplet impact. Thus, Eq. 16 becomes,

$$
\frac{\partial(\rho\mathbf{V})}{\partial t} + \nabla \cdot (\rho\mathbf{V}\mathbf{V}) = -\nabla p + \nabla \cdot \mu\left(\nabla\mathbf{V} + \nabla\mathbf{V}^T\right) + \sigma(T)K\nabla f + F_b
\tag{26}
$$

3.3   Heat Transfer and Solidification

We assume that solidification occurs at melting temperature and we neglect viscous dissipation. Densities of liquid and solid phases are assumed to be constant and equal to each other. The energy equation is then written,

$$
\frac{\partial h}{\partial t} + (V \cdot \nabla)h = \frac{1}{\rho}\nabla \cdot (k\nabla T)
\tag{27}
$$

Energy equation has two dependent variables; these are temperature T and enthalpy h. The method of Cao et al. (1989) may be employed to transform the energy equation in terms of enthalpy alone. The main advantage of this method is that it solves the energy equation for both phases simultaneously. The transformed energy equation is as follows (Cao et al. 1989),

$$
\frac{\partial h}{\partial t} + (V \cdot \nabla)h = \frac{1}{\rho}\nabla^2(\beta h) + \frac{1}{\rho}\nabla^2\phi
\tag{28}
$$

where in the solid phase,

$$h \leq 0; \quad \beta = \frac{k_s}{C_s}, \quad \phi = 0 \tag{29}$$

at the liquid-solid interface,

$$0 < h < H_f; \quad \beta = 0, \quad \phi = 0 \tag{30}$$

and in the liquid phase,

$$h \geq H_f; \quad \beta = \frac{k_l}{C_l}, \quad \phi = -\frac{H_f k_l}{C_l} \tag{31}$$

where ϕ is a new source term, and H_f is the latent heat of fusion. Subscripts l and s refer to liquid and solid properties, respectively. The energy equation has now only one dependent variable, the enthalpy, h. The relationship between temperature and enthalpy is,

$$T = T_m + \frac{1}{k}(\beta h + \phi) \tag{32}$$

where T_m is the melting point of the droplet. Heat transfer within the substrate is by conduction only. The governing equation is,

$$\rho_w C_w \frac{\partial T_w}{\partial t} = \nabla \cdot (k_w \nabla T_w) \tag{33}$$

where subscript w indicates the substrate. An adiabatic boundary condition was used at the free surface. Note that, initially, the dominant heat loss from the droplet is due to heat conduction to the substrate and, later on, conduction and convection to the solidified layer. Estimates of heat loss by convection from the droplet surface to the surrounding gas showed that it is three orders of magnitude lower than heat conduction to the substrate. Therefore, the adiabatic condition at the free surface is reasonable. This condition can, however, be easily modified to a convective, radiative, or mixed boundary condition.

3.4   Initial and Boundary Conditions

Initial conditions, i.e., droplet size, impact velocity, substrate and droplet temperatures, liquid-substrate contact angle, and thermal contact resistance, are given along with the thermophysical properties of the droplet and substrate. Heat conduction within the substrate is accounted for.

The incomplete contact between the drop and the substrate results in a temperature discontinuity across the contact surface. The effect can be incorporated in the model via definition of the thermal contact resistance, R_c (see Eq. 1). Values of R_c are provided as an input to this model. Although in principle R_c could vary with time and/or position on the interface, in this analysis, it was assumed to be constant. In practice, R_c typically varies between 10^{-7} and 10^{-6} m^2 K/W.

Computation of velocity field has to account for the presence of a moving, irregularly shaped solidification front on which the relevant boundary conditions are applied. The solidified regions are treated by a modified version of the fixed velocity method. In this approach, a liquid volume fraction Θ is defined such that $\Theta = 1$ for a cell completely filled with liquid, $\Theta = 0$ for a cell filled with solid, and $0 < \Theta < 1$ for a cell containing a portion of the solidification front. Normal and tangential velocities on the faces of cells containing only solidified material are set to zero. The modified continuity and momentum equations are then given by Pasandideh-Fard et al. (2002),

$$\nabla \cdot (\Theta \mathbf{V}) = 0 \tag{34}$$

$$\frac{\partial (\Theta \mathbf{V})}{\partial t} + (\Theta \mathbf{V} \cdot \nabla)\mathbf{V} = \frac{-\Theta}{\rho}\nabla p + \Theta v \nabla^2 \mathbf{V} + \frac{\Theta}{\rho}\mathbf{F}_b \tag{35}$$

$$\frac{\partial f}{\partial t} + (\Theta \mathbf{V} \cdot \nabla)f = 0 \tag{36}$$

The modified Navier-Stokes, volume of fluid, and energy equations are solved on an Eulerian, rectangular, staggered mesh in a 3D Cartesian coordinate system. Details of the computational procedure are described in Pasandideh-Fard et al. (2002).

3.5   Simulations of Droplet Impact

The model is first validated by comparing its predictions to experimental measurements of Aziz and Chandra (2000). Relevant properties for nickel, tin, and stainless steel are shown in Table 2. Figure 12 shows the spread factor ratio versus time for the impact of a 2.7 mm tin droplet impacting on a stainless steel substrate at 1 m/s and 513 K. The substrate temperature is 298 K and the melting point of tin is 505 K. As shown in the figure, the predictions are in excellent agreement with the experimental results as the resolution of the numerical calculations is increased to 27 cell per radius (CPR) or higher. Figure 13 shows a comparison between experimental measurements and numerical simulations of the impact of a tin droplet on a previously deposited and solidified tin splat (Ghafouri-Azar et al. 2004). The comparison between the predictions and experiments is again excellent for such a relatively complicated situation.

Table 2 Properties of nickel, alumina, and stainless steel. For substrate material (stainless steel), the only properties needed are density, thermal conductivity, and specific heat

Properties	Material			Tin	Stainless steel	
	Nickel					
Density [kg/m^3]	7.9E3			6.970E3	7.900E3	
Melting point [°C]	1453			232	–	
Heat of fusion [J/kg]	3.1E5			5.81E4	–	
Kinematic viscosity [m^2/s]	°C			2.756E-7	–	
	1453	6.7E-7				
	1577	5.7E-7				
	1627	5.4E-7				
	1727	5.0E-7				
Liquid thermal conductivity [W/(m.K)]	45			33.6	–	
Liquid specific heat [J/(kg.K)]	444			244	–	
Surface tension [N/m]	1.78			0.69	–	
Solid thermal conductivity [W/(m.K)]	°C			62.2	°C	
	527	67.6			127	16.6
					327	19.8
	727	71.8			527	22.6
	927	76.2			727	25.4
	1227	82.6			927	28.0
Solid specific heat [J/(kg.K)]	°C			210	°C	
	527	530			127	515
	727	562			327	557
	927	594			527	582
	1227	616			727	611
					927	640
					1227	682

3.5.1 Effect of Solidification on Breakup

Figure 14 shows the different stages of the normal impact of a 60 μm nickel droplet on a smooth stainless steel substrate at 290 °C (Pasandideh-Fard et al. 2002). The impact speed is 73 m/s and the initial droplet temperature is 1600 °C. Thermal contact resistance is assumed to be 10^{-7} m^{2}K/W. This case corresponds to Re = 7892, We = 1419, Ste = 1.67, and Pr = 0.043; hence, Ste/Pr = 38.3, which indicates the effect of solidification on droplet spreading is important. As droplet starts spreading, instabilities around the rim appear. These instabilities result in generation of a number of fingers as well as breakup of the finger tips into smaller drops (Fig. 14). Examination of the numerical results shows that, for this impact conditions, these instabilities occur due to solidification. This is demonstrated in Fig. 15. As the thermal contact resistance is increased by an order of magnitude (Fig. 15c), solidification occurs at a slower rate, and the splat assumes a circular disk shape. The effect of substrate temperature has been found to be of great importance in affecting the dynamics of the impact on metallic substrates (Dhiman et al. 2007).

Fig. 12 Spread factor versus time for a tin droplet impacting on a stainless steel substrate. Impact conditions: impact velocity 1 m/s, initial droplet temperature 513 K, substrate temperature 298 K, droplet diameter 2.7 mm, melting point of tin 505 K (Experimental points from Aziz and Chandra (2000)
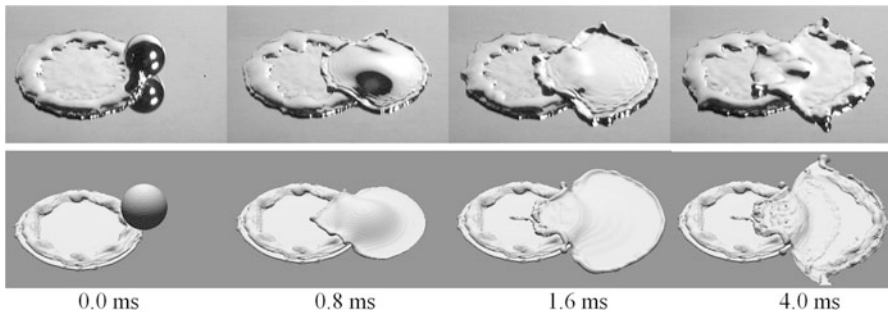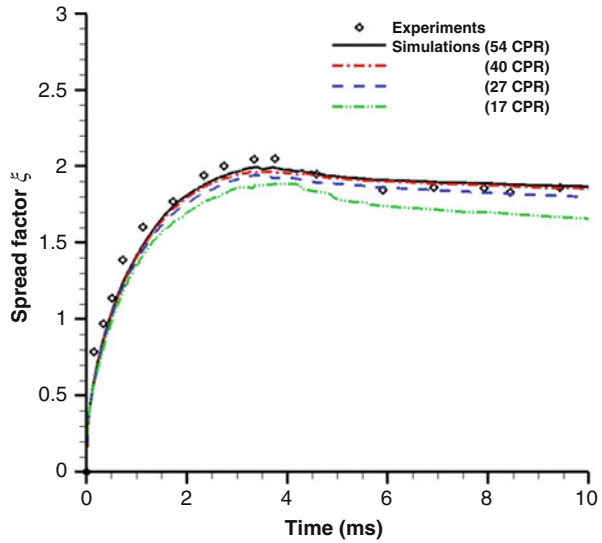

Fig. 13 Comparison of photographs and computer-generated images of a 2.2-mm-diameter tin droplet landing with a velocity of 2.5 m/s at a point 3.0 mm from the center of a solidified splat (Ghafouri-Azar et al. 2004)

3.5.2 Effect of Surface Roughness on Impact Dynamics

Raessi et al. (2005) and Parizi et al. (2007) studied the effect of surface roughness on the dynamics of droplet impact; silicon substrates were etched and patterned with cubes of 1, 2, and 3 um. The distance between the cubes was the same as their height. Figure 16 shows good agreement between the final splat shape of a nickel droplet impacting on the 1 um rough surface and the numerical predictions. For these patterned surfaces, as the roughness increases, the final splat shape is no longer circular (Fig. 17). This effect is particularly important for the case of 3 μm roughness. The effect is due to the fact that solidification rate depends on the direction of the spreading droplet. As shown in Fig. 17b, the calculation of the splat shape in the absence of solidification results in disk-like splat. Figures 18a, b show the contact area of the liquid droplet with the surface of the substrate. As shown, the contact is
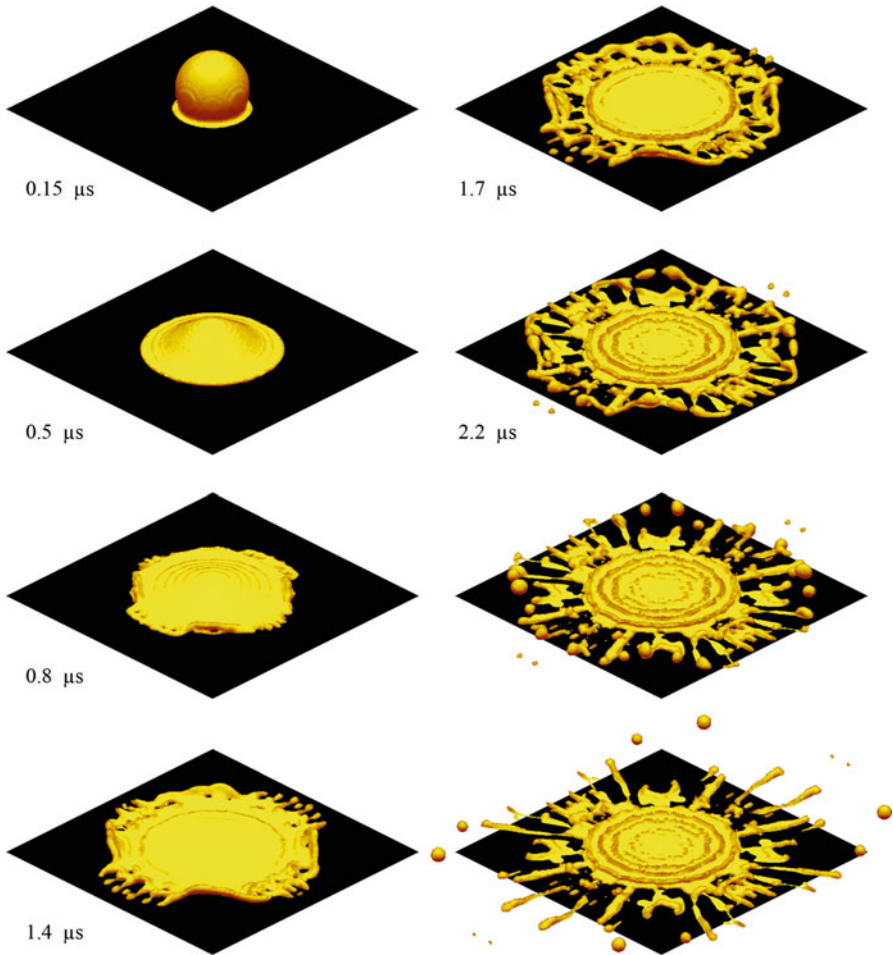
Fig. 14 Simulations showing the impact of a 60-μm-diameter molten nickel particle at 1600 °C landing with a velocity of 73 m/s on a stainless steel plate initially at a temperature of 290 °C. The contact resistance at the substrate surface was assumed to be 10^{-7} m²K/W (Adapted from Ghafouri et al. (2003))

maximum at an angle of 45°. Increased contact results in a faster rate of solidification; hence, the spreading is arrested quickly in the directions with high contact.

3.5.3   Impact of Partially Molten Droplets

Wu et al. (2009) and Alavi et al. (2012) studied the impact of partially molten zirconia and partially molten nickel droplets, respectively. The droplets are melted on the outer layer and have a solid core. This situation often occurs in thermal spray
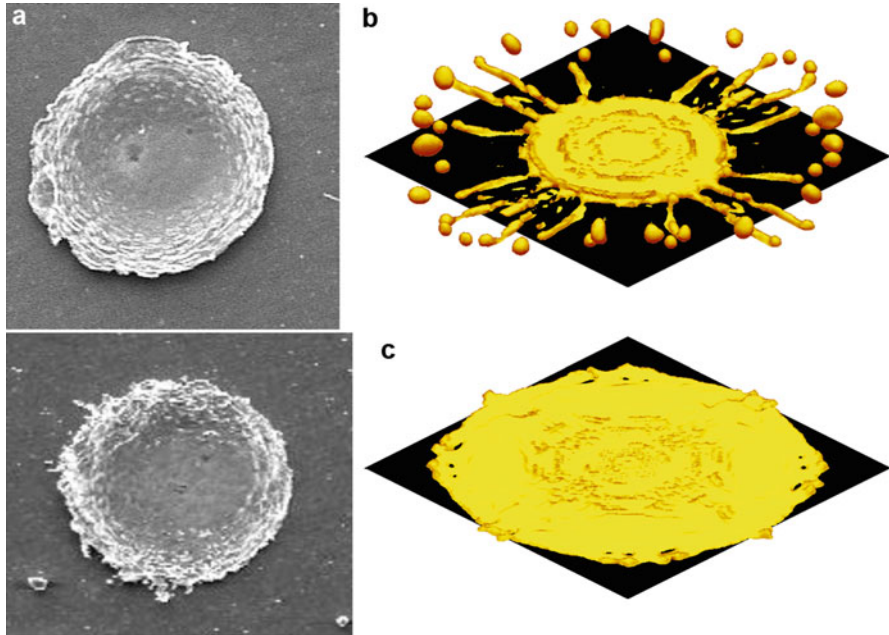
Fig. 15 Nickel splat shapes on a steel plate initially at 400 °C from (**a**) experiments, (**b**) numerical model assuming a contact resistance of 10^{-7} m^{2}K/W, and (**c**) numerical model assuming a contact resistance of 10^{-6} m^{2}K/W, (McPherson and Shafer 1982)

coating process when a particle is not heated sufficiently and does not fully melt. Insufficient heat transfer may be due to the trajectory of the particle as well as its big size.

Figure 19 shows the dynamics of the impact of a fully molten nickel droplet on a smooth, stainless steel substrate. Because of the high substrate temperature, solidification rate is rather slow and no splashing is observed. Upon impact, the drop starts spreading and solidifying. Some splashing is observed after around 1 μs after the impact. The final splat is shaped as a flat disk with raised rims. As the streamlines illustrate, vortices are generated in the gas flow during the particle impingement. These vortices influence the amount of the material detached from the particle during splashing. It may be noted that at 1 μs, in addition to the main vortex flow, another circulation is observed which is caused by the movement of the splashed droplet.

Figure 20 shows spreading of a partially molten nickel droplet. Compared to the fully molten case, the presence of the hard core results in a reduction in spreading and less splashing. Furthermore, because of the unmelted core, there is a bump in the center of the final splat. Alavi et al. (2012) show that increase in the impact speed will have no effect on the size of this bump, but will increase splashing and decrease the thickness of the final splat. A larger unmelted core promotes splashing.
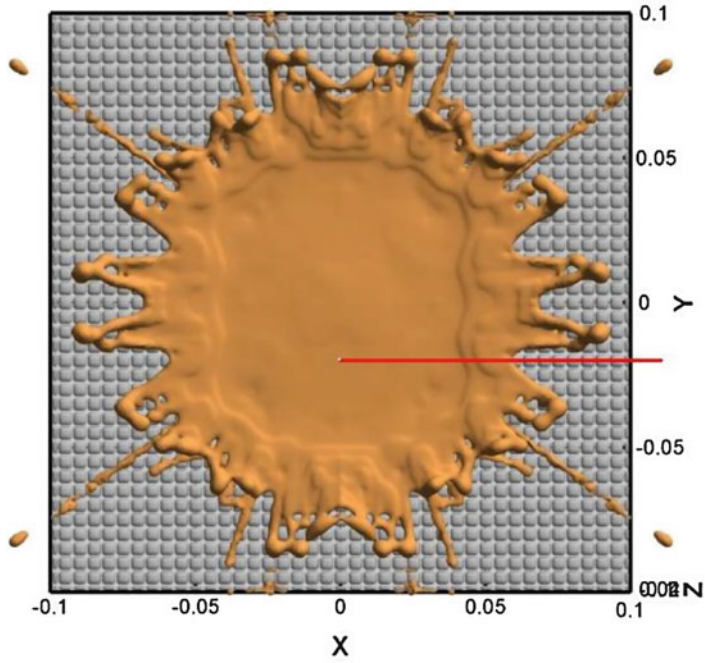
Columns: 1 μm high, 1 μm space
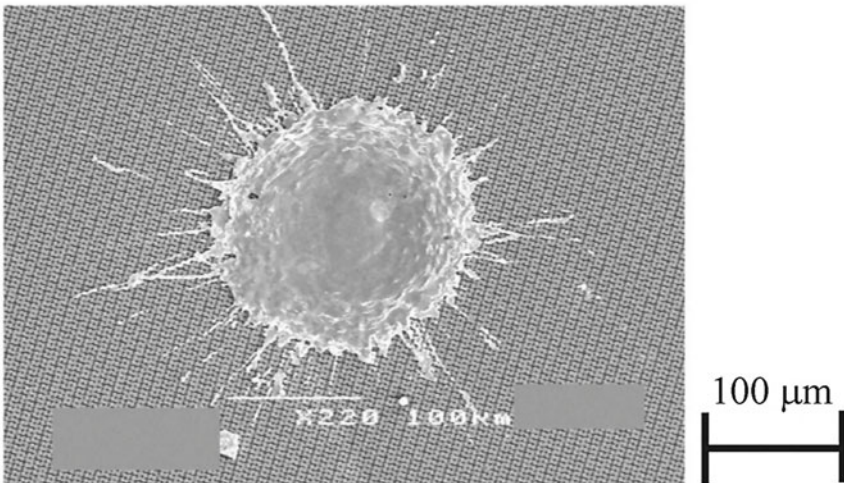
Final Diameter - 195 μm

Fig. 16 Effect of surface roughness on spreading of a nickel droplet on a silicon substrate (Monaghan 2012)
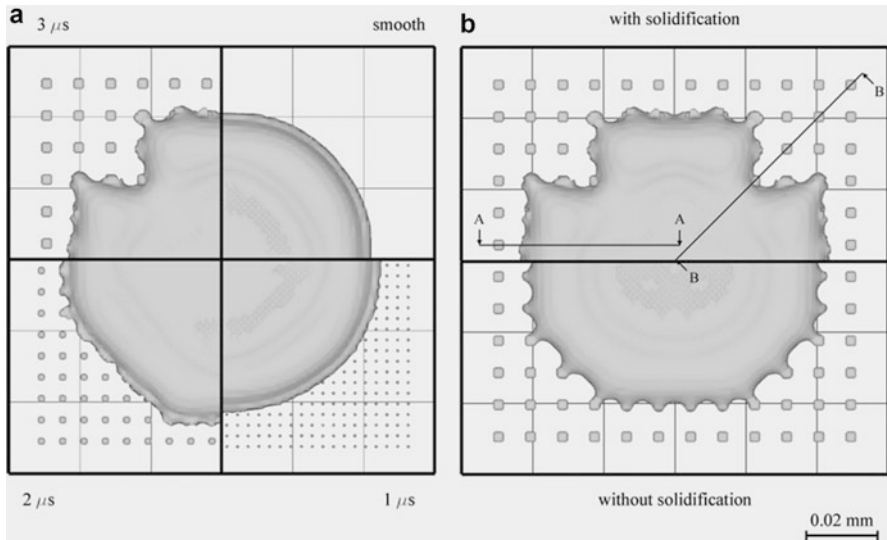
Fig. 17 Comparison between (**a**) the shape of alumina splats on different surface conditions in the presence of solidification and (**b**) splat shape on a substrate with 3 μm roughness and an alumina droplet on the same substrate and the corresponding time but without solidification. 40-μm-diameter alumina droplets at 2055 °C impacting with a velocity of 65 m/s onto alumina substrates initially at 25 °C and at different surface roughness (Mehdizadeh et al. 2005)
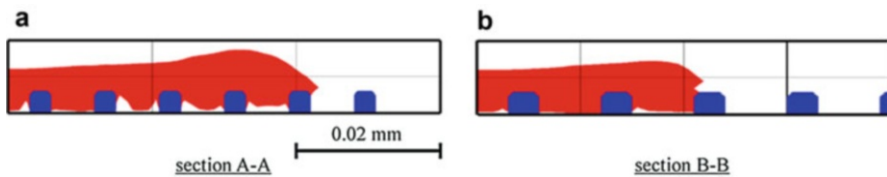

Fig. 18 Cross section of the alumina splat on a substrate with 3 μm roughness in the directions shown in Fig. 6b. The cubes on the substrate and the splat are shown in *blue* and *red*, respectively (Monaghan 2012)

3.6   Smoothed Particle Hydrodynamics (SPH)

Another promising method to study the impact and solidification of droplets and formation of a coating is the so-called smoothed particle hydrodynamics or SPH. The method was originally introduced and developed by Gingold and Monaghan (1977) and Lucy (1977). In SPH the computational domain is discretized using fluid particles. Each particle has density and mass to represent a lump of fluid moving around with the velocity of the fluid at that location in a Lagrangian manner. Properties of these particles are smoothed over a distance known as the smoothing
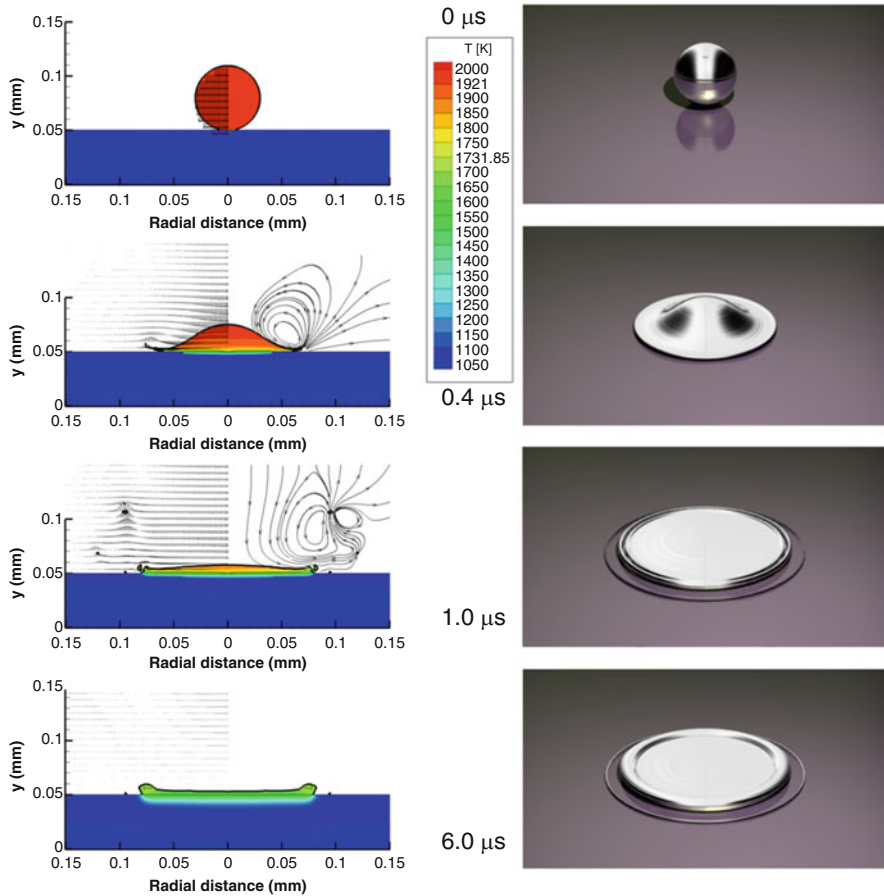
Fig. 19 Fully molten nickel particle, 60 μm; initial temperature, 1921 K; impact velocity, 100 m/s; substrate temperature, 1050 K; thermal contact resistance 10–6 m^2 K/W. The *thin black line* inside the particle shows the solidification front (Mundo et al. 1995)

length. This means that the properties of a particle of interest can be calculated from its neighboring particles. The contribution of neighbors is weighted using a kernel function that mostly depends on the distance between neighboring particles.

Since its inception, SPH has been extensively used in simulating different physical phenomena in fields like astrophysics, fluid sciences, oceanography, ballistics, etc. One of the major subjects studied in SPH is interfacial flows. Practical studies like tsunami simulations (Liu et al. 2008), simulation of floating bodies like ships (Cartwright et al. 2004), and multiphase studies (Hu and Adams 2006) are among them. In multiphase flows, numerical study of droplets has been of interest to many researchers due to applications in fields like spray coating and inkjet printing. Recently, Farrokhpanah et al. (2015) studied droplet impact on a surface and proposed and implemented a model for contact angle.
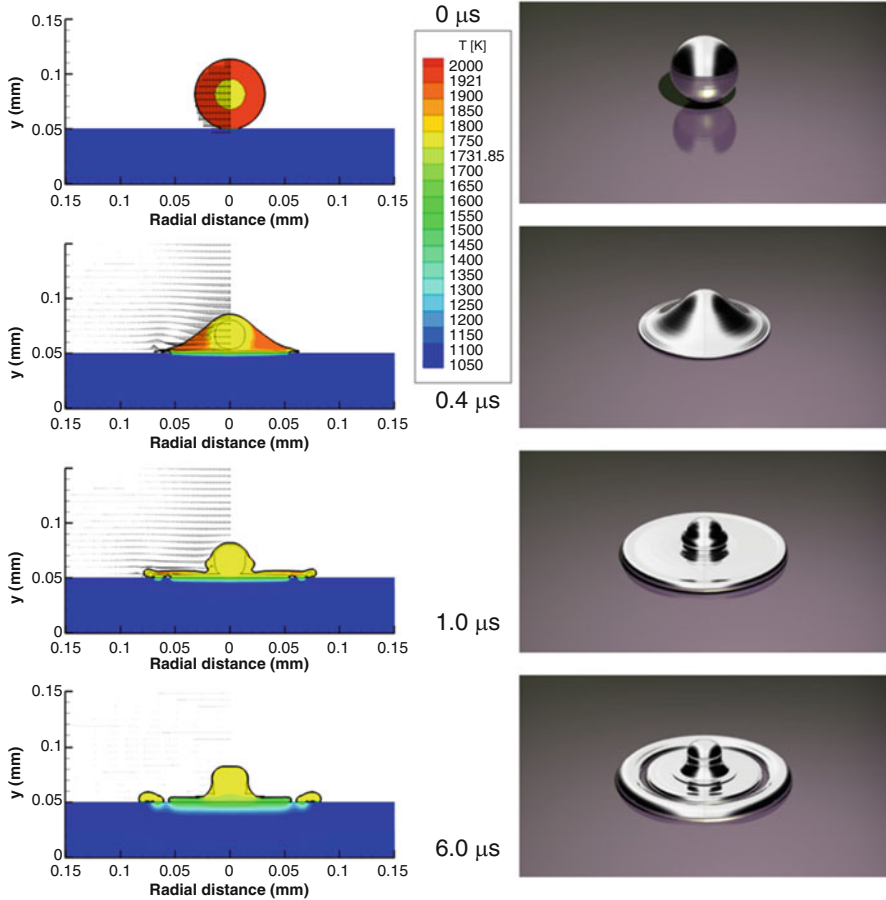
Fig. 20 Semi-molten nickel particle impact, 64 μm dia.; solid core dia, 28.7 μm; initial temperature, 1737 K; impact velocity, 100 m/s; substrate temperature, 1050 K; thermal contact resistance 10–6 m2 K/W. The *thin black line* inside the particle shows the solidification front (Mundo et al. (1995))

SPH solves Navier-Stokes equations in a Lagrangian framework. In this frame, Eqs. 15 and 16 for an isothermal case are,

$$\frac{D\rho}{Dt} = -\rho\nabla \cdot V \tag{37}$$

$$\frac{DV}{Dt} = \frac{1}{\rho}[-\nabla p + \nabla \cdot \bar{\bar{\tau}} + F_b + F_{ST}] \tag{38}$$

where $\frac{D}{Dt} = \frac{\partial}{\partial t} + V. \nabla$ is the substantial derivative, and F_b represents external body forces such as gravity. The surface tension force, F_{st}, is approximated based on the continuum surface force (CSF) model of Brackbill et al. (1992).

The continuity and momentum equations are closed by the equation of state, which calculates pressure using density in the form of (see Monaghan 2012),

$$P = P_0 \left(\frac{\rho}{\rho_0} \right)^\gamma + b \tag{39}$$

where $\gamma = 7$ and 1.4 for liquid and gas phases, respectively, b is a background pressure, and P_0 represents a reference pressure adjusted to keep maximum density deviations from ρ_0 in the order of O(1%).

In SPH, the local values of dependent variables are interpolated by an integral interpolant. For example, quantity A, which is a function of spatial coordinate system, may be exactly expressed,

$$A(r) = \int A(r')\delta(r - r')dr' \tag{40}$$

where r is spatial coordinates, dr' is the differential volume element, and δ is the Dirac delta function. The above may be approximated by a kernel, W,

$$A(r) = \int A(r')W(r - r', h)dr' \tag{41}$$

The kernel is defined,

$$\lim_{h \to 0} W(r - r', h) = \delta(r - r') \tag{42}$$

For a particle with mass m_i and density ρ_i at position r_i, the integral may be approximated by,

$$A_i = \sum_{j=1}^{N} m_j \frac{A_j}{\rho_j} W(r_i - r_j, h) \tag{43}$$

Also, gradient operator and others may be similarly approximated, e.g.,

$$\nabla A_i = \sum_{j=1}^{N} \frac{m_j}{\rho_j} (A_j - A_i) \nabla_i W_{ij}$$

where N is the total number of particles in the domain. In practice, the summation is limited to a limited number of particles which are in the neighborhood of particle i since W rapidly approaches zero with distance from particle i. The most commonly used kernel is the cubic spline, which, in one dimension, has the following form:
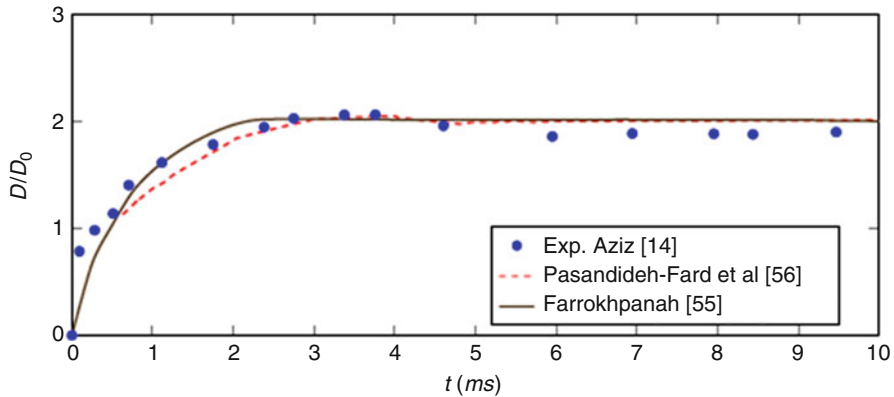
Fig. 21 Spread factor for a tin drop at 240 °C with 2.7 mm diameter impacting at 1 m/s on a 25 °C stainless steel substrate. *Solid line* (SPH), *dashed line* (VOF[55]), symbols (measurements[14])

$$W(x,h)/h = \begin{cases} \frac{1}{6}\left[(2-q)^3 - 4(1-q)^3\right]\}, & \text{for } 0 \le q \le 1 \\ \frac{1}{6}(2-q)^3, & \text{for } 1 \le q \le 2 \\ 0 & \text{for } q > 2 \end{cases} \qquad (44)$$

where $q = |x|/h$. For a detailed description of the application of SPH technique to fluid equations, the reader is referred to the review article by Monaghan (2012).

Farrokhpanah et al. presented a method for applying contact angle on a horizontal surface during the impact of a drop using SPH. The model is capable of accurately applying contact angle to a stationary and a moving contact line. In the method, the prescribed value of contact angle is used to adjust the interface profile near the triple phase point. This is done by adjusting the surface normally close to the contact line and interpolating the drop profile into the boundaries. Farrokhpanah et al. (2015) developed a parallel, GPU (graphic processing unit)-compatible SPH solver to capture interface evolution during droplet impact. To improve stability and performance of the solver, a customized reduction algorithm is used on the shared memory of GPU. Speedup using a variety of different memory management algorithms on GPU-CPU were studied. The algorithm was validated using the Rayleigh-Taylor instability test.

Figure 21 compares the predicted SPH results (Farrokhpanah 2016) for the spread factor with those obtained with VOF-based algorithm (Pasandideh-Fard et al. 2002) and by experimental measurement (Aziz and Chandra 2000). The comparison is very good.

4   Coating Buildup

Thermal spray deposition involves the impingement of a very large number of droplets that first land on a bare substrate and then, as the deposit grows thicker, on previously accumulated splats. The growing mass of the coating material on the

substrate loses heat by conduction to the substrate and by convection and radiation to the surrounding atmosphere. If incoming droplets add energy to the deposit faster than it is lost, the temperature of the metal will increase and the spray will land in a layer of molten metal. If heat transfer to the surroundings is sufficiently fast to allow droplets to cool down and freeze after impact, they will form solid splats. For a molten droplet to fuse with a solid deposit, it must have enough energy to cause remelting in the material under its impact point, which then solidifies again.

Ghafouri-Azar et al. (2003, 2004) studied the coalescence of 2.2-mm-diameter tin droplets deposited in lines on a substrate, each offset by a small amount from the other. Figure 22 shows splats formed by depositing four tin drops along a straight line, with the center of each drop offset by 2.0, 3.0, and 3.0 mm, respectively, from that of the previous one. They used numerical simulations to predict the shapes of splats formed by interacting droplets and to calculate where sufficient remelting occurred for splats to fuse with each other.

4.1   Porosity Formation

During spray deposition, molten droplets fuse together to form a solid layer that is not perfectly dense, but contain pores and cracks that may or may not be desirable, depending on the function of the coating. In general, low porosity is desirable since that increases the strength of the coating and makes it impervious. In some specialized applications, closed porosity may be desirable, such as in thermal barrier coatings, where the insulating properties are improved by the presence of air pockets. Several different mechanisms have been identified that can create porosity: curling up of splats due to thermal stresses, entrapment of gas under impacting particles, and incomplete filling of cavities in the already deposited coating. Protuberances may already exist on a rough substrate, or they may be created during spraying by the presence of unmelted particles in the spray, or as a result of satellite droplets detaching from impacting droplets and solidifying on the surface.

Pores formed by gas entrapment are typically very small and found at the interface between splats in thermal spray coatings. Based on transmission electron microscopy of plasma-sprayed coatings, McPherson and Shafer (1982) showed that the interfaces between lamellae consist of regions of perfect contact alternating with gaps of 0.01–0.1 μm which probably arise from absorbed or entrapped gas between impinging droplets and previously solidified layers.

Splat curl up is caused by residual stresses in the splat as it cools and shrinks after being sprayed on the surface. The bottom surface of the splat is attached to the substrate and cannot shrink, while the upper surface is free to contract. The resulting stresses are relieved either by the edges of the splat curling up or by generation of cracks. Fukanuma (1994) developed a model for porosity formation during thermal spray coating process by considering deformation of a molten particle and showed that most of the porosity is near the periphery of the splat, starting at a distance from its center of about 0.6 times the spat radius (R). Porosity

Fig. 22 Splats formed by depositing four 2.2-mm-diameter tin drops along a straight line, with the center of each drop offset by 2.0, 3.0, and 3.0 mm, respectively, from that of the previous one (Ghafouri-Azar et al. 2003)

First drop
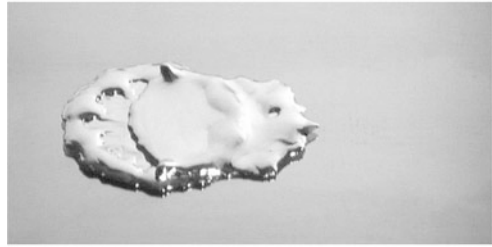
3 mm offset

3 mm offset

3mm offset

was sensitive to particle velocity, ambient gas pressure, particle diameter, and molten material viscosity.

Xue et al. (2007) studied the impact of molten droplets on a rough surface where liquid is driven into the crevices between asperities on the surface by liquid pressure, while surface tension restrains it from completely filling gaps, leaving voids. An analytical model was developed to calculate the volume of these voids that predicted, within an order of magnitude, the volume of voids measured from experiments.

4.2   Modeling Coating Formation

Thermal spray coatings are formed by the impact and deposition of millions of molten and semi-molten droplets on a substrate. While the impact of many droplets on a surface can be accurately modeled, it is not yet computationally possible to deposit millions of droplets using computational fluid dynamics and predict the microstructure of the coating. In order to develop such a model, based on Monte Carlo approach, Ghafouri-Azar et al. (2003, 2006) developed a three-dimensional model of coating formation. The model was further developed by Xue et al. (2007), (2008), and Parizi et al. (2010).

One of the promising modeling approaches for detail simulation of coating formation is smoothed particle hydrodynamics approach, first introduced by Gingold and Monaghan (1977) and Lucy (1977) in 1977. The method is Lagrangian and can handle many droplet impact events simultaneously in a very efficient manner.

The next two sections summarize the stochastic approach for predicting microstructure of coatings and the SPH approach, respectively.

4.2.1   Monte Carlo Simulations

Ghafouri-Azar et al. (2003, 2006) proposed a three-dimensional, stochastic model of thermal spray coating formation that can predict coating porosity and roughness as a function of spray parameters. The model assigns values of droplet size, velocity, and temperature T, dispersion angle and azimuthal angle to molten droplets on the substrate by generating random values of these properties, assuming that their properties follow known distributions with user-specified mean and standard deviation (Xue et al. 2008) that can be obtained for specific experiments by diagnostic instruments. Once the impact conditions of the individual droplet are selected from these distributions, the splat size is calculated by a simple analytical expression proposed by Aziz and Chandra (2000) (Eq. 9).

Interaction of an impacting droplet over a previously deposited splat was considered in the following manner. When a droplet lands overlapping a previously deposited splat, it will not spread into a disk-shaped splat but will assume a shape that depends on its distance from the center of the splat under it. Based on experimental results, and some detailed simulations of sequential droplet impact using a three-dimensional model, Ghafouri-Azar et al. (2003) developed four possible scenarios for the second splat shape formed by two-droplet interactions. To select one of these scenarios, the distances between the droplet impact point and the center points of all previously deposited splats were evaluated. The smallest distance was then used to determine the splat shape according to the rules that were established by approximating detailed numerical simulations of droplet interactions on a substrate and observations of interacting plasma-sprayed splats collected on a surface during experiments. The surface area of noncircular splats was assumed to be the same as it would have been had the splats remained circular.

According to Xue et al. (2006, 2007), porosity is formed because of the incomplete filling of the interstices on previously deposited splats, since surface tension prevents molten material from entering small gaps. The model assumes that the

impacting molten droplet is in contact with a series of uniform hemispherical asperities on the surface along the splat radius. In order to calculate the volume of the voids created between the hemispheres and the liquid layer, the equilibrium profile of the liquid meniscus is calculated using a method in which the total potential and surface energies of the system are minimized. Knowing the shape of the liquid meniscus and the profile of the asperity, one can use some geometrical expressions and then integrate the gap area over the total length of the splat to calculate the volume of the incompletely filled voids. In addition to curl up and incomplete filling of interstices, a third phenomenon may result in the formation of porosity. The small, satellite droplets which are formed when droplets splash and are settled on the surface also promote the formation of porosity. Based on this assumption, the number of satellite droplets, their sizes, and locations are approximated using the theories presented by Xue et al. (2008). These satellite droplets, in turn, create surface roughness and the incomplete filling of the coating layer will create more porosity.

Figures 23 and 24 show the result of the stochastic model for an yttria-stabilized zirconia plasma-sprayed coating (Xue et al. 2008). The calculations were based on
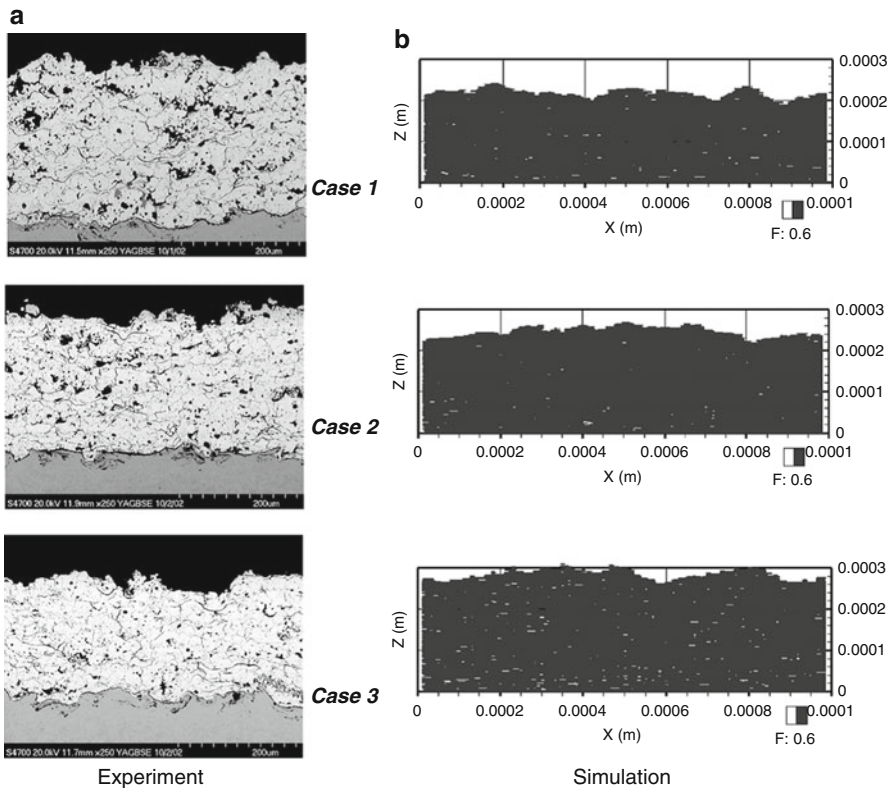

Fig. 23 Cross sections of three YSZ coating cases from (a) experiments (b) simulations
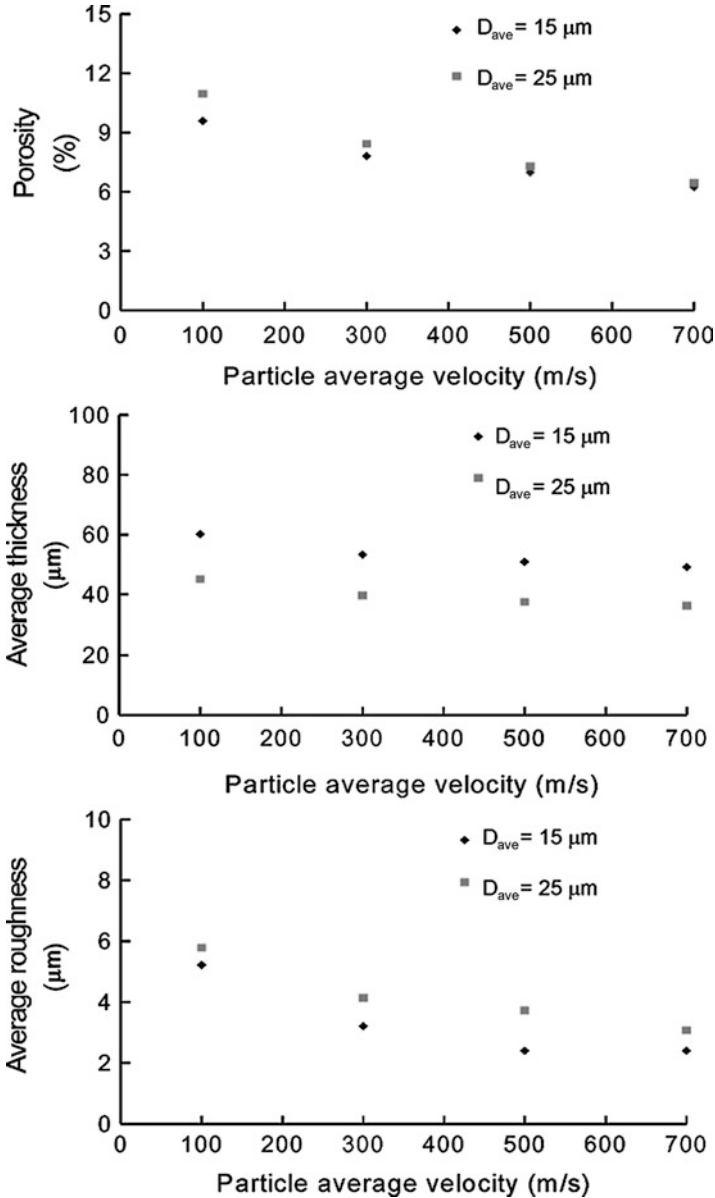
Fig. 24 Variations of coating porosity, average thickness, and average roughness with particle size and impact speed

the following spray parameters: average particle diameter and standard deviation of 25 μm and 5 μm, respectively; average particle temperature and standard deviation of 3000 K and 50 K, respectively; average impact speed and standard deviation of

100 m/s and 10 m/s, respectively; dispersion angle and standard deviation of 3.0 and 0.58°, respectively; and a uniform distribution in the azimuthal direction. The gun standoff distance was 0.12 m, and the average powder feed rate for the cases studied was 0.35 g/s. The gun moved constantly back and forth along the length of the substrate with a speed of 0.6 m/s. The model correctly predicts the effect of different operating parameters on coating porosity, roughness, and thickness (Xue et al. 2008).

Stochastic models are very useful in predicting microstructure of coatings as a function of operating conditions and show the dependence of porosity, roughness, and thickness on different parameters.

References

Afkhami S, Bussmann M (2008) Height functions for applying contact angles to 3D VOF simulations. Int J Numer Methods Fluids 61:827–847

Alavi S, Pasandideh-Fard M, Mostaghimi J (2012) Simulation of semi-molten particle impacts including heat transfer and phase change. J Therm Spray Technol 21:1278–1293

Aziz S, Chandra S (2000) Impact, recoil and splashing of molten metal droplets. Int J Heat Mass Transf 43:2841–2857

Bennett T, Poulikakos D (1994) Heat-transfer aspects of splat-quench solidification – modeling and experiment. J Mater Sci 29:2025–2039

Bertagnolli M, Marchese M, Jacucci G (1995) Modeling of particles impacting on a rigid substrate under plasma spraying conditions. J Thermal Spray Tech 4:41–49

Brackbill J, Kothe D, Zemach C (1992) A continuum method for modeling surface tension. J Comput Phys 100:335–354

Bussmann M (1999) PhD thesis, Department of Mechanical and Industrial Engineering, University of Toronto, 1999

Bussmann M, Mostaghimi J, Chandra S (1999) On a three-dimensional volume tracking model of droplet impact. Phys Fluids 11:1406

Bussmann M, Chandra S, Mostaghimi J (2000) Modeling the splash of a droplet impacting a solid surface. Phys Fluids 12:3121

Cao Y, Faghri A, Chang W (1989) A numerical analysis of Stefan problems for generalized multi-dimensional phase-change structures using the enthalpy transforming model. Int J Heat Mass Transf 32:1289–1298

Cartwright B, Groenenboom P, Mcguckin D (2004) Examples of ship motions and wash predictions by smoothed particle hydrodynamics. 9th international symposium on the practical design of ships and other floating structures

Cossali G, Coghe A, Marengo M (1997) The impact of a single drop on a wetted solid surface. Exp Fluids 22:463–472

Dhiman R, Chandra S (2005) Freezing-induced splashing during impact of molten metal droplets with high Weber numbers. Int J Heat Mass Transf 48:5625–5638

Dhiman R, McDonald A, Chandra S (2007) Predicting splat morphology in a thermal spray process. Surf Coat Technol 201:7789–8801

Farrokhpanah A (2016) Numerical solution to phase change problem: application to suspension plasma spray. PhD thesis, University of Toronto, 2016

Farrokhpanah A, Samareh B, Mostaghimi J (2015) Applying contact angle to a two dimensional multiphase smoothed particle hydrodynamics model. J Fluids Eng 137:041303–041301

Fauchais P, Fukumoto M (2004) Knowledge concerning splat formation: an invited review. J Therm Spray Technol 13:1–24

Fukanuma H (1994) A porosity formation and flattening model of an impinging molten particle in thermal spray coatings. J Therm Spray Technol 3:33–44

Fukanuma H, Ohmori A (1994) Behavior of molten droplets impinging on flat surfaces. In: Proceedings of the 7th national thermal spray conference, 563 (1994)

Fukomoto M, Huang Y (1999) Flattening mechanism in thermal sprayed Ni particles impinging on flat substrate surface. J Therm Spray Technol 8(3):427–432

Fukumoto M, Ohgitani I (2004) Effect of substrate surface change by heating on transition in flattening behavior of thermal sprayed particles. In: Lugscheider E, Berndt C (eds) Thermal spray: advances in technology and application. ASM International, Materials Park, pp 1–6

Ghafouri-Azar R, Shakeri S, Chandra S, Mostaghimi J (2003) Interactions between molten metal droplets impinging on a solid surface. Int J Heat Mass Transf 46:1395–1407

Ghafouri-Azar R, Mostaghimi J, Chandra S, Charmchi M (2003) A stochastic model to simulate the formation of a thermal spray coating. J Therm Spray Technol 12:54–69

Ghafouri-Azar R, Mostaghimi J, Chandra S (2004) Numerical study of solidification of a droplet over a deposited frozen splat. Int J Comput Fluid Dyn 18:133–138

Ghafouri-Azar R, Mostaghimi J, Chandra S, Charmchi M (2006) Development of residual stresses in thermal spray coatings. Comput Mater Sci 3:13–26

Gingold R, Monaghan J (1977) Smoothed particle hydrodynamics: theory and applications to non-spherical stars. Mon Not R Astron Soc 181:375–389

Hirt C, Nichols B (1981) Volume of fluid (VOF) method for the dynamics of free boundaries. J Comput Phys 39:201–225

Hu X, Adams N (2006) A multi-phase SPH method for macroscopic and mesoscopic flows. J Comput Phys 213:844–861

Inada S, Yang W (1994) Solidification of molten metal droplets impinging on a cold surface. Exp Heat Transfer 7:93

Jiang X, Wan Y (2001) Role of condensates and adsorbates on substrate surface on fragmentation of impinging molten droplets during thermal spray. Thin Solid Films 385:132–141

Kang B, Zhao Z, Poulikakos D (1994) Solidification of liquid-metal droplets impacting sequentially on a solid-surface. ASME J Heat Transfer 116:436–445

Kothe D (1998) Perspective on Eulerian finite volume methods for incompressible interfacial flows. In: Kuhlmann H (ed) Free surface flows. Springer, New York, pp 267–331

Li C, Li J, Wang W (1998) The effect of substrate preheating and surface organic covering on splat formation. In: Coddet C (ed) Proceedings of the 15th international thermal spray conference. ASM International, Materials Park, pp 473–480

Liu H, Lavernia E, Rangel R (1993) Numerical-simulation of substrate impact and freezing of droplets in plasma spray processes. J Phys D: Appl Phys 26:1900–1908

Liu V, Wang G, Matthys E (1995) Thermal analysis and measurements for a molten metal drop impacting on a substrate: cooling, solidification and heat transfer coefficient. Int J Heat Mass Transf 38:1387

Liu P, Yeh H, Costas S (eds) (2008) Advances in coastal and ocean engineering: advanced numerical models for simulating tsunami waves and runup. World Scientific Publishing Singapore 10

Lucy L (1977) A numerical approach to the testing of the fission hypothesis. Astron J 82:1013–1024

Madejski J (1976) Solidification of droplets on a cold surface. Int J Heat Mass Transf 19:1009

McDonald A, Lamontagne M, Moreau C, Chandra S (2006) Impact of plasma-sprayed metal particles on hot and cold glass surfaces. Thin Solid Films 514:212–222

McDonald A, Moreau C, Chandra S (2007) Thermal contact resistance between plasma-sprayed particles and flat surfaces. Int J Heat Mass Transf 50:1737–1749

McPherson R, Shafer B (1982) Interlamellar contact within plasma-sprayed coatings. Thin Solid Films 97:201–204

Mehdizadeh N, Raessi M (2004) Effect of substrate temperature on splashing of molten tin droplets. ASME J Heat Transfer 126(3):445–452

Mehdizadeh N, Lamontagne M, Moreau C, Chandra S, Mostaghimi J (2005) Photographing impact of molten molybdenum particles in a plasma spray. J Thermal Spray Technol 14:354–361

Monaghan J (2012) Smoothed particle hydrodynamics and its diverse applications. Annu Rev Fluid Mech 44:323–346

Mostaghimi J, Pasandideh-Fard M, Chandra S (2002) Dynamics of splat formation in plasma spray coating process. Plasma Chem Plasma Process 22:59–84

Mundo C, Sommerfeld M, Tropea C (1995) Droplet-wall collisions: experimental studies of the deformation and breakup process. Int J Multiphase Flow 21:151–173

Osher S, Fedkiw R (2001) Level set methods: an overview and some recent results. J Comput Phys 169:463–502

Parizi H, Rosenzweig L, Mostaghimi J, Chandra S, Coyle T, Salimi H, Pershin L, McDonald A, Moreau C (2007) Numerical simulation of droplet impact on patterned surfaces. J Therm Spray Technol 16:713–721

Parizi H, Mostaghimi J, Pershin L, Jazi H (2010) Analysis of the microstructure of thermal spray coatings: a modeling approach. J Therm Spray Technol 19:736–744

Pasandideh-Fard M, Mostaghimi J (1996) On the spreading and solidification of molten particles in a plasma spray process: effect of thermal contact resistance. Plasma Chem Plasma Process 16S: S83–S98

Pasandideh-Fard M, Qiao Y, Chandra S, Mostaghimi J (1996) Capillary effects during droplet impact on a solid surface. Phys Fluids 8:650

Pasandideh-Fard M, Bhola R, Chandra S, Mostaghimi J (1998) Deposition of tin droplets on a steel plate: simulations and experiments. Int J Heat Mass Transf 41:2929–2945

Pasandideh-Fard M, Chandra S, Mostaghimi J (2002a) A three-dimensional model of droplet impact and solidification. Int J Heat/Mass Transf 45(1):2229–2242

Pasandideh-Fard M, Pershin V, Chandra S, Mostaghimi J (2002b) Splat shapes in a thermal spray coating process: simulations and experiments. J Therm Spray Technol 11:206–217

Pech J, Hannoyer B (2000) Influence of substrate preheating monitoring on alumina splat formation in DC plasma process. In: Berndt CC (ed) Proceedings of the 1st international thermal spray conference. ASM International, Materials Park., 2000, pp 759–765

Pershin V, Lufitha M, Chandra S, Mostaghimi J (2003) Effect of substrate temperature on adhesion strength of plasma-sprayed nickel coatings. J Therm Spray Technol 12:370–376

Poirier D, Poirier E (1994) Heat transfer fundamentals for metal casting, 2nd edn. Minerals, Metals and Materials Society, Warrendale, pp 41–42

Raessi M, Mostaghimi J, Bussmann M (2005) Droplet impact during the plasma spray coating process – effect of surface roughness on splat shapes. In: Proceedings of 17th international symposium on plasma chemistry, Toronto, pp 916–917

Raessi M, Mostaghimi J, Bussmann M (2007) Advecting normal vectors: a new method for calculating interface normal and curvatures when modeling two-phase flows. J Comput Phys 226:774–797

Rioboo R, Tropea C, Marengo M (2001) Outcomes from a drop impact on solid surfaces. Atomization Sprays 11:155–165

Trapaga G, Mathys E, Valencia J, Szekely J (1992) Fluid-flow, heat-transfer, and solidification of molten-metal droplets impinging on substrates – comparison of numerical and experimental results. Metall Trans B 23B:701–718

Watanabe T, Kuribayashi I, Honda T, Kanzawa A (1992) Deformation and solidification of a droplet on a cold substrate. Chem Eng Sci 47:3059

Worthington A (1876) A second paper on the forms assumed by drops of liquids falling vertically on a horizontal plate. Proc R Soc London 25:498

Worthington A (1907) The splash of a drop. The Society for Promoting Christian Knowledge, London. 1907

Wu T, Bussmann M, Mostaghimi J (2009) The impact of partially molten YSZ particle. J Therm Spray Technol 18:957–964

Xu L, Zhang W, Nagel S (2005) Drop splashing on a dry smooth surface. Phys Rev Lett 94:184505

Xu L, Barcos L, Nagel S (2007) Splashing of liquids: interplay of surface roughness with surrounding gas. Phys Rev E 76:066311

Xue M, Chandra S, Mostaghimi J (2006) Investigation of splat curling up in thermal spray coatings. J Therm Spray Technol 15:531–536

Xue M, Chandra S, Mostaghimi J, Salimijazi H (2007) Formation of pores in thermal spray coatings due to incomplete filling of crevices in patterned surfaces. Plasma Chem Plasma Process 27:647–657

Xue M, Chandra S, Mostaghimi J, Moreau C (2008) A stochastic model to predict the microstructure of plasma sprayed zirconia coatings. Model Simul Mater Sci Eng 16:065006

Zhang H, Wang X (2001) Studies of splat morphology and rapid solidification during thermal spraying. Int J Heat Mass Transf 44:579–4592

Zhao Z, Poulikakos D, Fukai J (1996a) Heat transfer and fluid dynamics during the collision of a liquid droplet on a substrate. 1. Modeling. Int J Heat Mass Transf 39:2771–2789

Zhao Z, Poulikakos D, Fukai J (1996b) Heat transfer and fluid dynamics during the collision of a liquid droplet on a substrate. 2. Experiments. Int J Heat Mass Transf 39:2791–2802